INSTITUT NATIONAL DE RECHERCHE EN INFORMATIQUE ET EN AUTOMATIQUE

Automated Analysis of Basal Ganglia Intensity Distribution in Multisequence MRI of the Brain - Application to Creutzfeldt-Jakob Disease

Marius George Linguraru — Miguel Ángel González Ballester — Eric Bardinet — Damien Galanaud — Stephane Haïk — Baptiste Faucheux — Jean Jaques Hauw — Patrick Cozzone — Didier Dormont — Jean-Philippe Brandel — Nicholas Ayache

N° ????

May 2004

Thème ?

ISSN 0249-6399

Automated Analysis of Basal Ganglia Intensity Distribution in Multisequence MRI of the Brain - Application to Creutzfeldt-Jakob Disease

Marius George Linguraru* , Miguel Ángel González Ballester * , Eric Bardinet † , Damien Galanaud ‡ § , Stephane Haïk ¶ ‖ , Baptiste Faucheux ¶ ‖ , Jean Jaques Hauw ¶ ‖ , Patrick Cozzone § , Didier Dormont ‡†, Jean-Philippe Brandel ¶ , Nicholas Ayache *

Thème ? —
Projet EPIDAURE

Rapport de recherche n° ???? — May 2004 — 45 pages

Abstract: We present a method for the analysis of basal ganglia (including the thalamus) for accurate detection of human spongiform encephalopathy in multisequence MRI of the brain. One common feature of most forms of prion protein infections is the appearance of hyperintensities in the deep grey matter area of the brain in T2-weighted MR images. We employ T1, T2 and Flair-T2 MR sequences for the detection of intensity deviations in the internal nuclei. First, the MR data is registered to a probabilistic atlas and normalised in intensity. Then smoothing is applied with edge enhancement. The segmentation of hyperintensities is performed using a model of the human visual system. For more accurate results, a priori anatomical data from a segmented atlas is employed to refine the registration and remove false positives. The results are robust over the patient data and in accordance to the clinical ground truth. Our method further allows the quantification of intensity distributions in basal ganglia. The caudate nuclei are highlighted as main areas of diagnosis of sporadic Creutzfeldt-Jakob Disease (CJD), in agreement with the histological data. The algorithm permitted to classify the intensities of abnormal signals in sporadic CJD patient FLAIR images with a more significant hypersignal in caudate nuclei (7/7) and putamen (4/7) than in thalami.

* EPIDAURE Research Project - INRIA, Sophia Antipolis, France
† CNRS UPR640-LENA, Paris, France
‡ Department of Neuroradiology, La Pitié Salpêtrière Hospital, Paris, France
§ CRMBM UMR CNRS 6612, Faculty of Medicine, Marseille, France
¶ INSERM U360, National Reference Cell of Creutzfeldt-Jakob Diseases, La Pitié Salpêtrière Hospital, Paris, France
‖ R. Escourolle Neuropathological Laboratory, La Pitié Salpêtrière Hospital, Paris, France

Key-words: Brain MRI, multisequence MRI, grey matter, internal nuclei, Creutzfeldt-Jakob Disease, image registration, image normalisation, segmentation, human visual system

Analyse automatique de la distribution des intensités des noyaux gris centraux en IRM multiséquences du cerveau - Application à la maladie de Creutzfeldt-Jakob

Résumé : Nous présentons une nouvelle méthode d'analyse des noyaux gris centraux afin de faciliter le diagnostic des l'encéphalopathies spongiformes humaines a partir d'IRM cérébrales multiséquences. L'apparition des signaux hyper-intenses au sein des noyaux gris centraux dans les IRM pondérées en T2 est un point commun entre la majorité des formes des maladies à prions. Les séquences IRM T1, T2, et FLAIR-T2 sont utilisées pour la détection des point aberrants dans les noyaux gris centraux. Tout d'abord, les images sont recalées sur un atlas probabiliste et normalisées en intensité. Un filtrage anisotrope est ensuite appliqué afin de préserver les contours. Les signaux hyper-intenses sont extraits par un algorithme qui s'inspire d'un modèle psychovisuel humain. Pour plus de précision, des informations a priori sur l'anatomie issues d'un atlas segmenté permettent d'affiner le recalage et d'éliminer les faux positifs. Les résultats sont robustes et conformes aux observations fournies par les cliniciens. La méthode permet en outre une quantification de la distribution des intesités des noyaux gris centraux. Les noyaux caudés sont designés comme principales zones d'interêt diagnostic dans la Maladie de Creutzfeldt-Jakob (MCJ) sporadique, conformement aux données histologiques. La méthode a permis, de plus, de classer sans ambiguïté l'intensité des anomalies de signal chez les patients atteints de MCJ sporadique avec un hypersignal plus FLAIR marqué dans les noyaux caudés (7/7) et parfois les putamen (4/7) que dans les thalami.

Mots-clés : IRM du cerveau, IRM multiséquence, substance grise, ganglions de la base, maladie Creutzfeldt-Jakob, recalage d'images, normalisation, segmentation, système visuel humain

Contents

1 Context and Objectives **4**
1.1 Magnetic Resonance Imaging 5
1.2 CJD and MRI 6
1.3 Addressing the Problem 8

2 Pre-Processing **9**
2.1 Data 9
2.2 Image Normalisation 9
2.2.1 Spatial Normalisation 10
2.2.2 Intensity Normalisation 11
2.3 Noise Removal and Image Enhancement 12

3 Segmentation and Refined Registration **15**
3.1 A Priori Anatomical Data 16
3.2 Detection of Internal Nuclei and Refined Segmentation 16
3.3 Human Visual System 20

4 Results **22**
4.1 Paris Data 22
4.2 Marseille Data 30
4.3 ADC Analysis 30

5 Discussions **33**

6 Conclusion **39**

1 Context and Objectives

The identification of early diagnosis markers is a major challenge in the clinical care of patients with Creutzfeldt-Jakob Disease (CJD). This disease raises a number of questions to neuroradiological centres, due to the limited available knowledge that connects it to medical imaging. Some recent studies [4, 12, 17, 41] found strong correspondences between CJD patients and signal activation in the deep grey matter internal nuclei in Magnetic Resonance Imaging (MRI) of the brain. Since CJD is extremely aggressive, detecting the earliest signs of the disease becomes essential in studying its evolution.

This work is completed as part of the GIS-Prions Project, a national project funded by the French Ministry of Health, as a response to the increasing worries regarding the spread and evolution of the Prion protein infection-based diseases. Its goal is to develop techniques for the early detection and classification of various types of CJD, be it sporadic, new variant, genetic or iatrogenic [4, 5]. Besides assisting to better understand the disease evolution, our study aims to improve the early diagnosis of CJD envisaging the application

of a prospective treatment. The project involves several research centres across France and a database aiming to include CJD patients from two main neuroradiological centres in Paris and Marseille in the period between April 2002 and April 2004.

1.1 Magnetic Resonance Imaging

Magnetic Resonance Imaging (MRI) has become a leading technique widely used for imaging soft human tissue. Its applications are extended over all parts of the human body and it represents the most common visualisation method of human brain. Images are generated by measuring the behaviour of soft tissue under a magnetic field. Under such conditions, water protons enter a higher energy state when a radio-frequency pulse is applied and this energy is re-emitted when the pulse stops (a property known as resonance) [18]. A coil is used to measure this energy, which is proportional to the quantity of water protons and local biochemical conditions. Thus, different tissues give different intensities in the final MR image. From the brain MRI perspective, this quality makes possible the segmentation of the three main tissue classes within the human skull: grey matter (GM), white matter (WM) and cerebrospinal fluid (CSF). Their accurate segmentation remains a challenging task in a clinical environment.

The relative contrast between brain tissues is not a constant in MR imaging. In most medical imaging applications, little can be done about the appearance of anatomically distinct areas relative to their surroundings. In MRI, the choice of the strength and timing of the radio-frequency pulses, known as the MRI sequence [33], can be employed to highlight some type of tissue or image out another, according to the clinical application. However, the presence of artefacts due to magnetic field inhomogeneity (bias fields) and movement artefacts may hamper the delineation of GM versus WM and CSF and make their depiction difficult.

There is an entire family of MRI sequences that are used in common clinical practice. T1-weighted MRI offers the highest contrast between the brain soft tissues. On the contrary, T2-weighted and Proton Density (PD) images exhibit very low contrast between GM and WM, but high contrast between CSF and brain parenchyma. In other MRI sequences, like the Fluid Attenuated Inversion Recovery (FLAIR) sequence, the CSF is eliminated from the image in an adapted T1 or T2 sequence. More about these specific MRI sequences and their variations can be found in [6]. Multisequence MRI analysis combines the different information provided by the employed sequences. Combining such knowledge gives substantially more information about brain anatomy and possible occurring changes.

MR images depict a 3D volume where the organ or part of the body of interest is embedded. This information can be used to build a 3D representation of the structure of interest. This applies both to 2D sequences, where images are acquired in slices, and to recently developed 3D sequences, where the data are captured in the 3D Fourier space, rather than each slice being captured separately in the 2D Fourier space [33, 6].

In the next section we will focus on the use of MRI for the detection and classification of Creutzfeldt-Jakob diseases.

1.2 CJD and MRI

MRI is commonly used for non-invasive examinations of patients with neurological diseases. For the last fifteen years, evidence of MRI hypersignals in patients suffering from CJD has been found. However, the observations and studies describing its ability to help in the diagnosis of CJD are in an early stage. Most of the studies are concerned with sporadic CJD cases, which represent 80% of all forms of CJD. The first study cases describe activations in T2-weighted images (and FLAIR T2 images) with higher incidence in the basal ganglia (see Figure 1) in a bilateral symmetric form [14, 25, 29]. Schroeter [31] conducts a large study on sporadic CJD patients and concludes that the MR sensitivity in detecting CJD is 67% with a specificity of 93%. No anomalies are generally reported in T1-weighted images of sporadic CJD patients, with some exceptions, such as in [10].

A great concern in the scientific world has been the occurrence and rapid increase in the number of cases of new-variant CJD in the 1990s, a form of human environmentally-acquired CJD. This type of CJD related to the bovine spongiform encephalopathy shows a different distribution of hyperintensities in brain MRI. In FLAIR and T2 sequences, abnormal high signals are depicted in the thalamus (see Figures 1 and 2). The sensitivity of MRI in diagnosing new-variant CJD is reported as 78% with a specificity of 100%. Unlike the sporadic cases, the new-variants have higher intensities in the thalamus when compared to putamen [9, 16].

Other forms of prion infections are genetic, such as Fatal Familial Insomnia (FFI) and Gertsmann-Straussler-Scheinker syndrome (GSS), or iatrogenic CJD, which are much less studied in MR imaging. The rarity of such cases makes them difficult to interpret from a statistical point of view. An overview of the clinical aspects of human spongiform encephalopathies can be found in [4].

Although the intensity of abnormal signals probably changes over time with the evolution of the disease, there are cases where no increase is noted or even no hypersignals appear in the internal nuclei. As mentioned above, cortical hypersignals are also associated with CJD, but on a much more reduced scale. Abnormal cortical signals are best detected in Diffusion Weighted Images (DWI) [2]. Areas of high signal in DWI are usually associated with a decreased apparent diffusion coefficient (ADC) value. Although there are overlaps between bright areas in FLAIR/T2 and in DWI, the MR sequences depict different types of abnormal pathological features.

There are several hypotheses relating hyperintensities in MRI and CJD. In [11, 35], correlation between MRI studies and neuropathological data shows that an elevation of signal in MRI T2-weighted sequences correlates with gliosis in pathological analysis. In [40, 41] it is also argued that hyperintensities in thalamus related to the variant CJD seem more likely linked to the level of gliosis than to spongiosis or prion deposits. Bahn and Parchi [3] relate the high signal in DWI to spongiform changes. More recently, Ha\"ik et al. [17] noted that, in a sporadic and a variant CJD cases, there is no clear association between the high MRI signal and gliosis or spongiform changes, but seems to be closer related to the accumulation of prion protein. Still, the relation between the prion deposits and strong signal in MRI remains ambiguous.

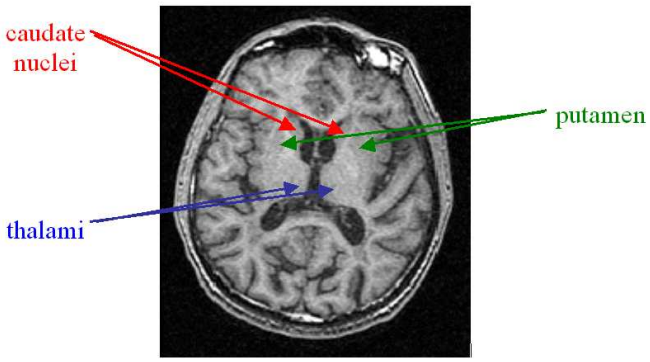

Figure 1: A map of deep grey matter internal nuclei in a normal T1 weighted axial MR image. The red arrows point towards the caudate nuclei, while blue and green arrows indicate the thalami and the putamen respectively.

Despite the given advances in the detection of CJD, to date, clear diagnosis can only be performed post-mortem. In-vivo pathological examinations could rarely be carried out through brain biopsy to confirm the diagnosis of CJD. However, brain biopsy is a risky invasive procedure with far from perfect results, since it is dependent on the brain sampling area. Through recent advances in the description of MRI abnormalities related to CJD, MRI is considered an essential tool in CJD diagnosis.[13, 25, 26] make MR related image processing an important tool in non-invasive CJD diagnosis. However, the interpretation of MR images is usually limited to a visual inspection performed by the medical staff and could lead to an under- or overestimation of the true incidence of CJD [5]. At present time, MRI is not included as a diagnosis criterion for sporadic CJD, although, as argued in our results and discussion sections, it presents valuable information to the clinician. It would be certainly useful to include MRI in the diagnosis of sporadic CJD, as for the variant forms [41]. Therefore, the necessity to further explore the advantages of Computer Aided Diagnosis (CAD) techniques in the MRI clinical environment becomes obvious.

Leemput [36] proposes a method for automated quantification of MR intensity changes in images of patients suffering from CJD. He acknowledges as common difficulties in processing such images the limited resolution, partial volume effects, noise, low contrast and intensity inhomogeneities, whether this is performed by the computer or the human expert. Hence, low level segmentation methods are inappropriate for the detection of hyperintensities in the affected areas of the brain. A mixture model of normal distributions combined with the expectation-maximisation algorithm (EM) is proposed. However, the method does not detect signal abnormalities in most of the CJD cases, while showing significant amounts of false positives (FP) along the interface between grey matter (GM) and cerebrospinal fluid (CSF).

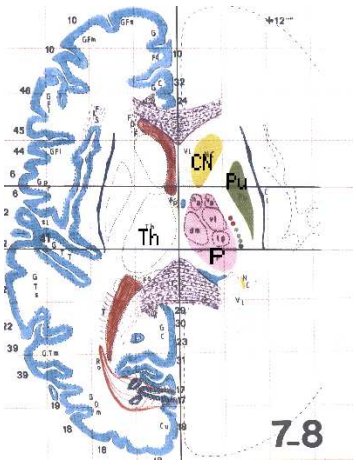

Figure 2: A map of deep grey matter internal nuclei reproduced from Talairach and Tournoux atlas [34]. The caudate nuclei (CN) are shown in yellow, the putamen (Pu) in green and the thalami (Th) in magenta. The pulvinar (P) is located in the posterior section of the thalamus

1.3 Addressing the Problem

Little is known about the early evolution of CJD patients. Most of the studied cases are of patients severely affected by the disease, as there is poor evidence of Prion infection at an early stage of the disease. Early detection of CJD is essential for better understanding of this lethal disease and for a shorter path towards finding its treatment. Likewise, little is known about possible ways to visualise and represent signs of CJD in conventional medical imaging.

Computer Assisted Diagnosis (CAD) algorithms have been introduced in clinical settings and automatic computerised methods to assist clinicians in detecting and characterising diseases are being developed. Their utility in a large number of clinical applications has been proven by multiple studies. They simplify the complex laborious tasks of every day clinical work, assist in the routine of investigating large numbers of medical images (which makes the human factor prone to errors) and present a valuable second opinion in decision making. Given the present knowledge and limitations in analysing medical images, namely MRI of the brain, for CJD related applications, we aim to detect Prion infections at an early stage and with the requested robustness and reliability desired in clinical applications.

The motion artefacts found in the set of images we work with (exemplified in Section 4) makes the use of statistical detection algorithms very difficult. Such algorithms rely on finding consistent repeatable signs of a disease over a set of patients [20, 21, 37]. Also, they need good contrast between GM and WM in T1-weighted images for stochastic analysis

according to a general atlas context. This is another major source of errors in cases of CJD, where patients suffer of severe dementia with often uncontrolled movements. In Figure 10 we note the contrast between soft brain tissues in a typical T1 image versus a typical T1 of a patient suffering from CJD.

The approach we propose is based on the use of a priori anatomical knowledge in the form of an accurately segmented and labelled image (e.g. the Zubal Atlas [42]) for precise segmentation and of a probabilistic atlas for intra- and inter-patient analysis. A feature detection technique based on a model of the Human Visual System (HVS) is employed for the depiction of hyper-signals. The remaining of this paper is organised as follows: Section 2 presents the complex pre-processing steps applied to the input images before the effective segmentation of disease activations. This includes spatial and intensity normalisation, atlas alignment and noise removal by anisotropic diffusion. Section 3 introduces the refined registration of internal nuclei using a segmentation atlas. Then we present the HVS-based detector, an adaptive thresholding method following the functioning of the human eye, that is used to segment abnormalities in deep grey matter. Some results of our method are illustrated in Section 4, before discussions and conclusion in Section 5.

2 Pre-Processing

In this section we will review the pre-processing stages used before the actual segmentation of CJD hypersignals. This is a simplified model of data normalisation and regularisation, which is required to put the images in the same general framework. The main advantage of image normalisation is the drastic reduction of the number of parameters. We further expand on these steps.

2.1 Data

The image acquisition protocol is designed to include three MRI sequences for each patient. As mentioned above, we can extract different kinds of information from each sequence relevant to our application. The sequences used by our algorithm are: a T1-weighted acquisition for its higher contrast between GM and WM and higher image resolution; T2-weighted images for the good contrast between the CSF and the brain parenchyma; and a T2-weighted FLAIR sequence, well-established for the depiction of CJD related activation in the brain. We use the T1 sequence to find the first estimate of the transformation for the registration process, the T2 for segmentation of CSF and brain and the FLAIR for segmentation of bright abnormalities in basal ganglia.

2.2 Image Normalisation

The large variability inherent to human anatomy and imaging parameters leads us to consider spatial and intensity normalisation as an approach to normalise patient images for further abnormality detection. This is done both for localising the areas of interest with the

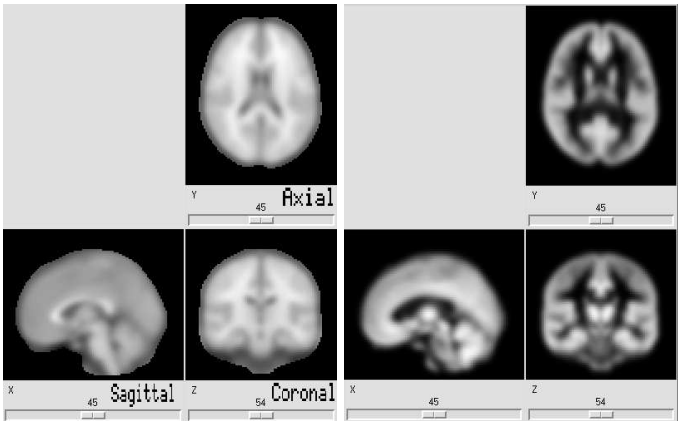

Figure 3: The MNI template. On the left, the probabilistic MNI atlas of the brain; on the right, the corresponding GM atlas. Please note the arrangement of MR images in radiological convention with an axial, a sagittal and a coronal view. This convention is reflected in figures throughout the paper.

help of an atlas of the brain, but also for normalising specific imaging parameters for an automatic detection of the affected brain areas. Furthermore, inter-patient analysis could now be performed.

2.2.1 Spatial Normalisation

Data registration to an atlas has become a common technique with the introduction of popular statistical algorithms for image processing, such as Statistical Parametric Mapping (SPM) [1] or Expectation Maximization Segmentation (EMS) [37]. A well-known probabilistic atlas in the scientific community is the MNI Atlas from the Montreal Neurological Institute at McGill University [8]. It was built using over 300 MRI scans of healthy individuals to compute an average brain MR image, the MNI template, which is now the standard template of SPM and the International Consortium for Brain Mapping [24]. The averaging is performed for the entire brain, but also on isolated GM, WM and CSF, providing a tool for statistical segmentation. For these reasons, we chose the MNI template as the basis for image alignment in our approach. Figure 3 shows the MNI template.

We propose the following registration scheme. T1 images have the highest resolution in our data set, hence we register them to the MNI template first using an affine transformation. The registration algorithm, previously developed in our group, is described in [28]. It uses a block matching strategy in a two-step iterative method. The standard assumption behind the algorithm is that there is a global intensity relationship between the template image and the one being registered to it. The method proposes several types of correlation measures:

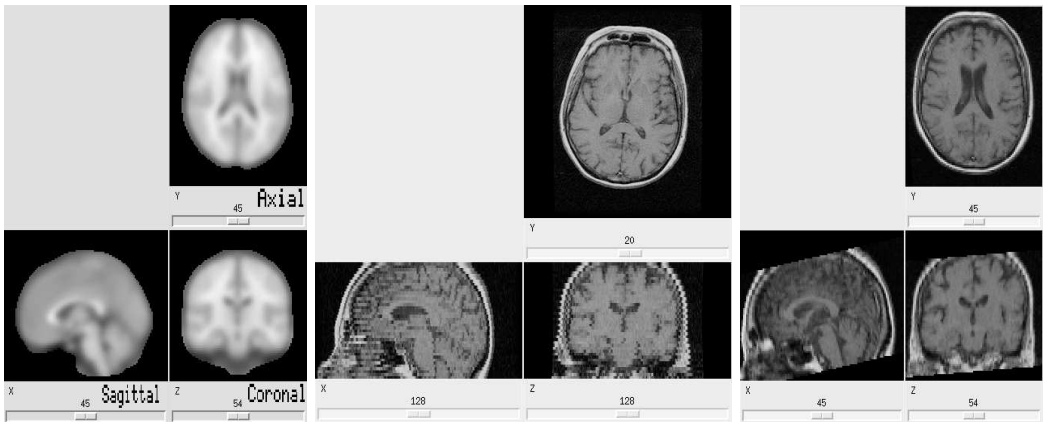

Figure 4: An example of spatial normalisation. The image on left shows the MNI template; the middle image is the subject's T1 before registration; the right image is the subject's T1 after spatial normalisation.

linear, functional or statistical. Using one of these, the correlation coefficient in our case, the transformation between the two images is computed block by block and a displacement field is thus generated. A parametric transformation, either affine or rigid, is then estimated from this deformation field. To further improve robustness, this procedure is repeated at multiple scales. More details can be found in [27].

Next, rigid intra-patient registration of all sequences is performed using the same algorithm as above. Both the T2 and the FLAIR images are registered to the T1 image. By combining this rigid transformations with the affine transformation matching T1 and MNI template, we can find correspondences between the atlas and the T2 and FLAIR images. This is illustrated in Figure 5. The final image resolution is that of the MNI atlas: 91x109x91 voxels. Figure 4 shows an example of spatial normalisation. With all images registered to the atlas, intra- and inter-patient analysis becomes simple and statistical algorithms can be applied.

2.2.2 Intensity Normalisation

In addition to geometric variability, MR images may also exhibit intensity variations. Contrast differences over a set of images are a common problem in image analysis. One can note considerable variations between images of different patients, but also in images of the same patient taken at different times. This makes identical anatomical parts of the imaged area appear with different intensities from one image to the next. As a result, it is difficult to tune processing parameters for robust repeatable results. To overcome problems, we propose the use of an intensity normalisation algorithm for the FLAIR images, prior to the detection

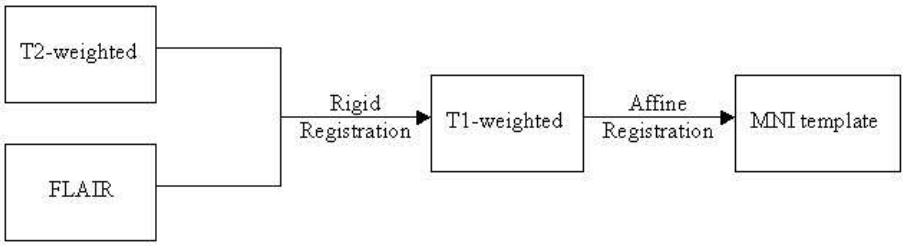

Figure 5: Diagram of the spatial normalisation algorithm. Intra-patient images are rigidly registered on the corresponding T1. The T1-weighted image is affinely registered to the atlas template. The resulting transformation is used to align all other MR images to the atlas.

of signal deviations. Our method performs an affine equalisation using the joint histogram of two images: a standard image onto which we align the intensity distribution of a second input image [30].

The two images must be registered prior to normalisation in intensity to align anatomical coordinates for the best use of the joint histogram between the two images. Ideally, the joint histogram will be as close as possible to a straight line along the first diagonal of the intensity plane, which is the result we aim to achieve with the affine intensity equalisation. In practice, a joint histogram between MR images of different subjects following the same acquisition protocol looks like a cloud of points centered around a line ($y = ax+b$) in the intensity surface. The affine equalisation we employ finds the parameters a and b by minimising the criterion C in equation 1, where i relates to the points of coordinates (x_i, y_i). Figure 7 shows an example of intensity normalisation between the MR images of two patients. Next in Figure 6 we can note the change in the joint histogram of the images shown in 7 before and after intensity normalisation.

$$C = \left(\sum_i \frac{|y_i - (a + bx_i)|}{\sqrt{1 + b^2}} \right) \tag{1}$$

2.3 Noise Removal and Image Enhancement

MR images are noisy. Our application aims to detect areas of abnormal intensity in the deep grey matter of the brain and noise can hamper the segmentation process. Thus, it seems natural to smooth our images in order to remove unwanted noise. However, we must ensure that the areas of interest (areas of high intensity) are preserved for accurate segmentation. Therefore, an edge-preserving blurring technique is required. Anisotropic diffusion offers the tool to perform image smoothing with edge enhancement, as our application necessitates. Figure 8 illustrates the direction of maximal and minimal diffusion of

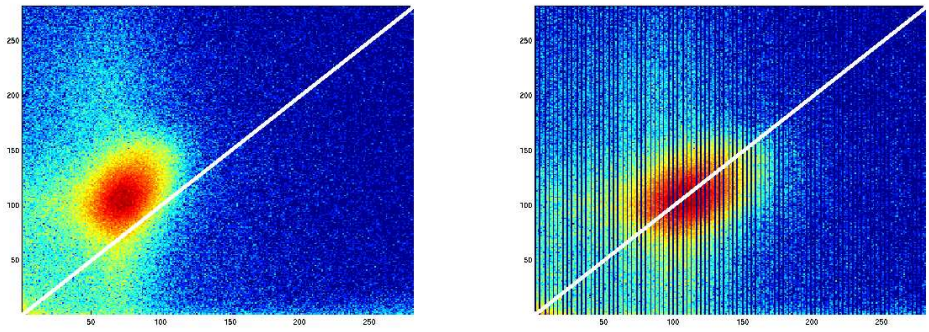

Figure 6: The joint histograms of the two MR patient images in Figure 7 before intensity normalisation (left) and after the affine regularisation of intensities (right). We note the realignment of the cloud of points in the middle of images to fit better the first diagonal (shown in white) once the image normalisation has been performed. The dark lines appearing in histogram of normalised images are caused by the dilation of the range of values in the image to be normalised; as we work with discrete data and we do not employ any interpolation, the affine normalisation will not cover the entire range between the minimum and maximum values leading to this visual artefact.

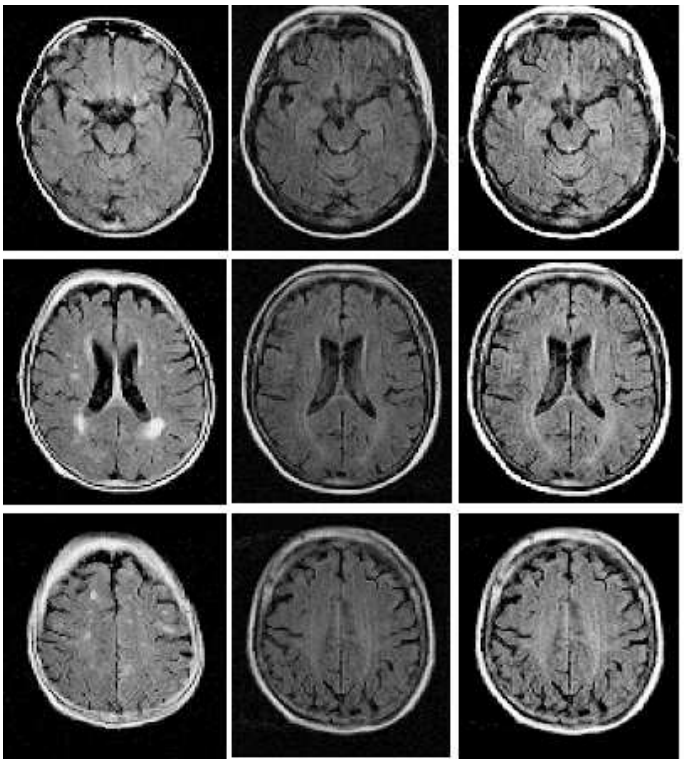

Figure 7: An example of intensity normalisation on FLAIR images. On the left column, three axial MR cross-sections of the first subject are shown; in the middle are the cross-sections of the second subject before normalisation; on the right column are the cross-sections of the second subject normalised in intensity with respect to the first subject.

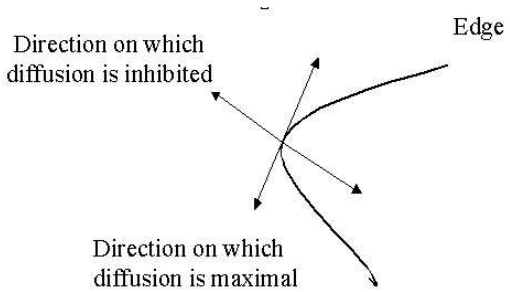

Figure 8: The anisotropic diffusion eigenvectors of the diffusion tensor. Smoothing is allowed along the edge, while inhibited across the margin.

the nonlinear anisotropic diffusion model introduced by Weickert [38]. This model uses a diffusion tensor with has two orthonormal eigenvectors (instead of a diffusivity function) that determine the direction of diffusion. Smoothing will take place along edges, but will be inhibited across boundaries. The choice of related eigenvalues determines the behaviour of the feature detector. We employ a strong decreasing diffusivity-like function that encourages strong smoothing within contours, while contrast at edges is enhanced. Equation 2 shows the eigenvalue (λ) corresponding to the eigenvector across the edge, where I is the image to diffuse.

$$\lambda = \begin{cases} 1 & |\nabla I_\sigma| = 0, \\ 1 - \exp\left(\frac{-1}{(|\nabla I_\sigma|/k)^{12}}\right) & |\nabla I_\sigma| > 0 \end{cases} \tag{2}$$

A few parameters are involved in the diffusion process, namely the scale of the Gaussian used to smooth at each iteration (σ), the number of iterations over which smoothing is done (t) and the contrast (k) which determines the presence of an edge. We employ a kernel for the Gaussian of size 5x5 (to smooth only small areas in images that have already small resolution) over 5 iterations, when the contrast approximates the mean of the image gradient (to ensure the stability of more significant edges in the image). We show an example of image diffusion in Figure 9. After diffusion, images have a better Signal-to-Noise Ratio (SNR) and small registration errors are also corrected.

3 Segmentation and Refined Registration

Our analysis is based on the abnormal MR intensities that can appear in the basal ganglia (including the thalamus) of patients suffering from CJD. To be able to segment GM and WM in MRI sequences, a good contrast between these types of tissues in T1-weighted images is desired. Figure 10 shows a typical T1 with high contrast between brain's soft tissues and a

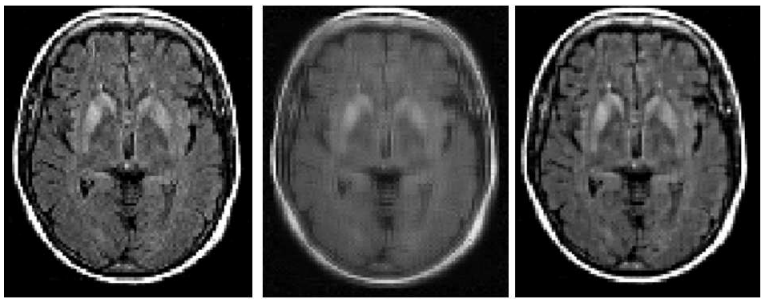

Figure 9: The effect of anisotropic versus linear diffusion on image smoothing. On the left, we show the original image from a patient with typical CJD activations in the basal ganglia; in the middle, the linearly diffused (Gaussian convolution) image after 5 iterations; on the right,the anisotropically diffused image after 5 iterations with smooth areas and well-preserved edges.

common T1 image from our database. Under the given circumstances, the segmentation of GM (where CJD affections are visible) cannot be done directly from the patient images. The MNI atlas can provide a probabilistic segmentation of GM, but this is not precise enough for our application. We use instead a segmented anatomical atlas of the brain, the Zubal Phantom [42], which is introduced in the next section.

3.1 A Priori Anatomical Data

The Zubal atlas offers a precisely labelled segmentation of brain structures from the T1-weighted MR image of one single subject. Our interest focuses on the internal nuclei, which are segmented in the phantom. First, the atlas must be aligned to our set of images, which have been previously registered to the MNI atlas. Thus, we register the Zubal Phantom to the MNI template, again using our block matching algorithm [28], to estimate an affine transformation. However, in order to preserve the correct values of the segmentation labels posterior to the application of the transformation, nearest-neighbour interpolation is performed, as opposed to the case of patient image registration, which employed spline interpolation. Figure 11 shows the results of registering the Zubal Phantom to the MNI reference without disrupting the Zubal labels.

3.2 Detection of Internal Nuclei and Refined Segmentation

Once the Zubal Phantom is registered to the working framework, we can easily depict the brain structures that are of interest, namely the deep GM internal nuclei. Reports in the literature [4, 12, 17, 40, 41] mention the importance of analysing MR intensities in the basal ganglia. Hence, we create a mask with the thalamus, putamen and head of the caudate -

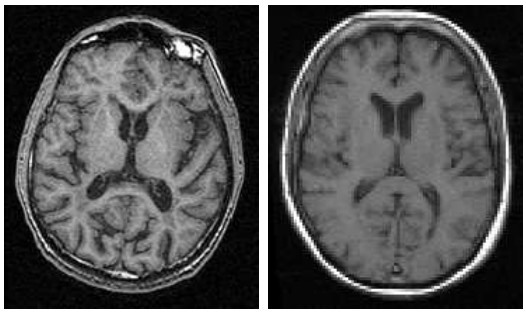

Figure 10: A typical T1-weighted MR image with good contrast between brain GM, WM and CSF (left) versus a T1 image from our data set (right).

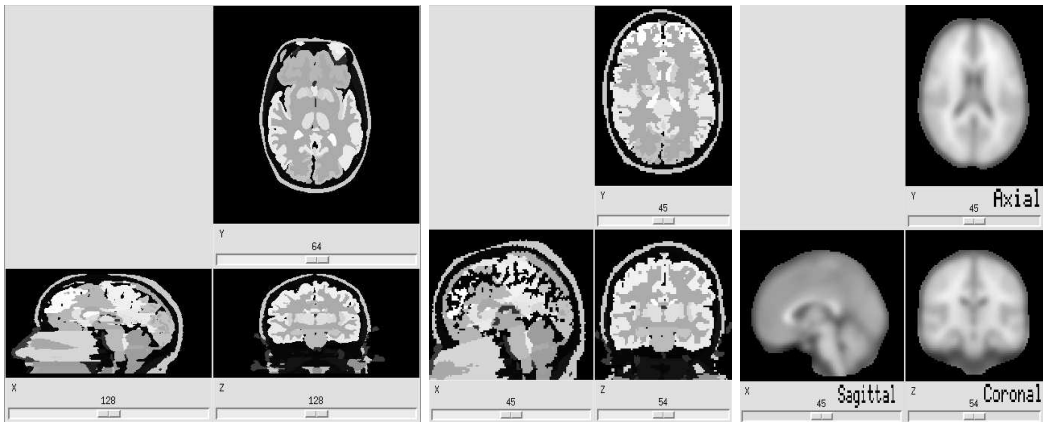

Figure 11: The registration of Zubal Phantom onto the MNI template. On the right, the original Zubal Phantom is shown; in the middle, we have the registered Zubal Phantom on the MNI template, which is shown in the right image.

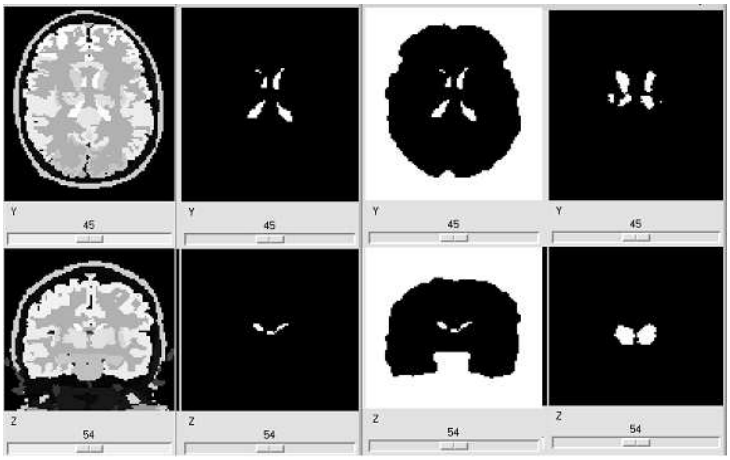

Figure 12: The segmentation of the Zubal Phantom. From left to right: column 1, the Zubal Phantom registered on MNI; column 2, the ventricles segmented from the Zubal Phantom; column 3, the cortex outer boundary is added to the ventricles; column 4, the internal nuclei segmented from the Zubal Phantom.

which will be referred as internal nuclei for the rest of this paper - from the Zubal Phantom registered on MNI (Figure 12). We aim to use this mask for the segmentation of internal nuclei in patient images. Although the affine registration gives correct correspondences in a general brain registration framework, the anatomical variability between patients makes the correspondence between the Zubal internal nuclei mask and the corresponding internal nuclei in each patient erroneous. A refinement of the registration in the deep GM between the Zubal internal nuclei mask and the patient internal nuclei seems necessary to allow us to use the a priori anatomical information resulting from the segmentation of the Zubal Phantom.

The segmentation of internal nuclei in patient images is not an obvious task; this is why we exploit the Zubal Phantom. Nevertheless, there are other important anatomical landmarks in the brain that are easier to identify. We concentrate on the segmentation of ventricles and cortex external boundary. Ventricles will give a good approximation of the deformation field around the internal nuclei, whereas the cortex boundary will impose the global spatial correspondence and stabilise the deformation field inside the brain. Figure 12 illustrates the segmentation of ventricles, brain contour and internal nuclei from the registered Zubal Phantom.

To obtain similar images of segmented brain margin and ventricles for each patient, we employ morphological opening on patient T2 images. The strong contrast that CSF has against the brain in T2-weighted images allows us to segment the ventricles, while the cortex boundary can be extracted from either T1 or T2 sequences. We prefer using the T1

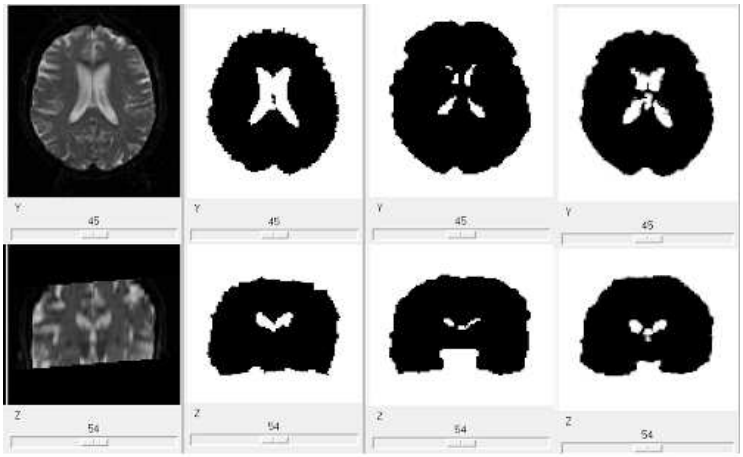

Figure 13: Registration of the Zubal ventricle and cortex outer boundary on a patient with very large ventricles. This is the most difficult case encountered, due to the patient's brain atrophy and the significant dilation of ventricles, next to the small ventricles in the Zubal Phantom, where the subject is young. The algorithm gives robust results, as seen above. From left to right: column 1, the T2 image of the patient registered on MNI; column 2, the ventricles and brain margin of the patient (ventricles segmented from T2 and cortex from T1); column3, the ventricles and brain boundary of Zubal Phantom; column 4, the ventricles and cortex boundary of the Zubal Phantom registered on the patient.

sequence, since the T2 image we employ lacks some top and bottom slices. The ventricles being located in the middle of the brain, it is correct to extract them from T2 images, but the cortex would be incomplete. We now are in the possession of two binary maps of ventricles and brain boundaries for each patient: one from the Zubal Phantom and the other from the patient. Non-rigid registration is used to align the two images, employing the algorithm described in [7]. Figure 13 shows typical results and Figure 14 shows the 3D deformation fields related to the registration in Figure 13. The outer margin of the cortex ensures that the deformation fields are spatially sound and do not pull the internal nuclei over their location.

Having the deformation fields computed, we apply them to the mask of internal nuclei of the Zubal Phantom, deforming the mask according to the position and size of the ventricles in the patient image. A diagram of the algorithm is shown in Figure 15. The deformed mask is used to segment the internal nuclei of the patient, mainly the putamen, head of the caudate and thalamus, areas associated with strong signals in the diagnosis of CJD. Figure 16 shows an example of registration of internal nuclei in 3D and the internal nuclei segmentation results in a T1-weighted MR image of a patient. A segmentation of internal

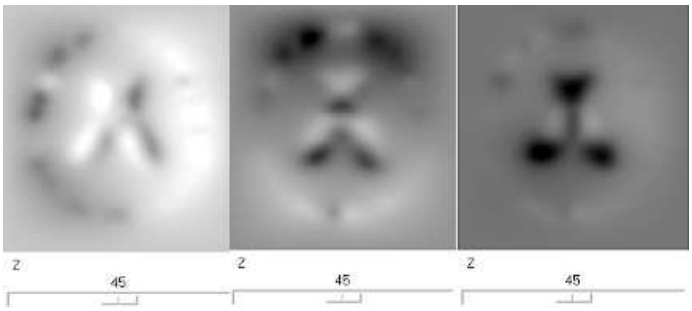

Figure 14: Deformation fields of the non-rigid registration between the Zubal Phantom ventricles and those of a patient with very large ventricles. On the left is the x field, the y field is in the middle column and the z field on the right.

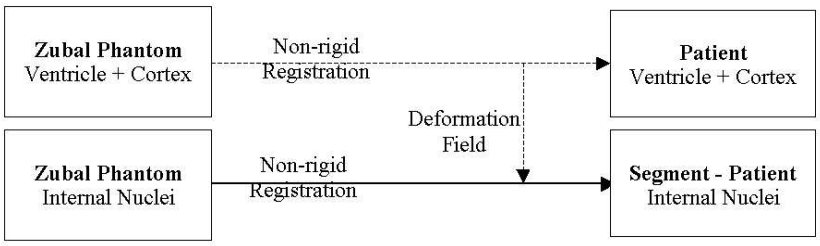

Figure 15: Diagram of the refined registration of internal nuclei.

nuclei is essential in discarding possible false positives in the detection of hyperintensities. More will be presented about it in the results section.

3.3 Human Visual System

The detection of areas of CJD activation in the brain is completed by a foveal segmentation algorithm. This is in essence a method of adaptive thresholding, which uses a mathematical model of human vision. Its motivation comes from the better sensitivity and specificity that the human eye has over classical algorithms in detecting and characterising image features. Figure 17 shows the variation of the threshold C_{min}adopted in our model over the variations in image intensity. $C_{classic}$ represented a classical non-adaptive threshold. A simplified model for the computation of $C_{min}$is shown in equation 3, where $c_{mpc}$is the minimal perceivable contrast, b is constant, $\mu_N$the mean value of the intensity of neighbourhood and μ_Aa mean weighted value of neighbourhood and background (entire image). The model is presented in greater detail in [23].

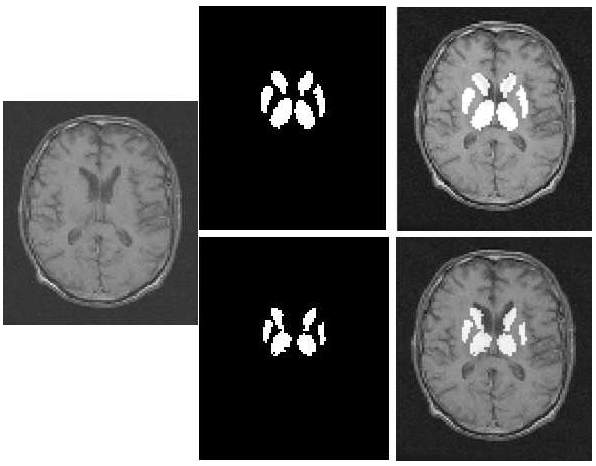

Figure 16: An example of internal nuclei registration and their segmentation in a T1-weighted image of the patient. On the left, we have the T1 image of the patient; in the middle column the internal nuclei maps; on the right, we show the segmentation of internal nuclei according to the binary map. The rows show: top - before non-rigid deformation with the head of the caudate superposed on the ventricles, bottom - after non-rigid deformation, showing an accurate segmentation.

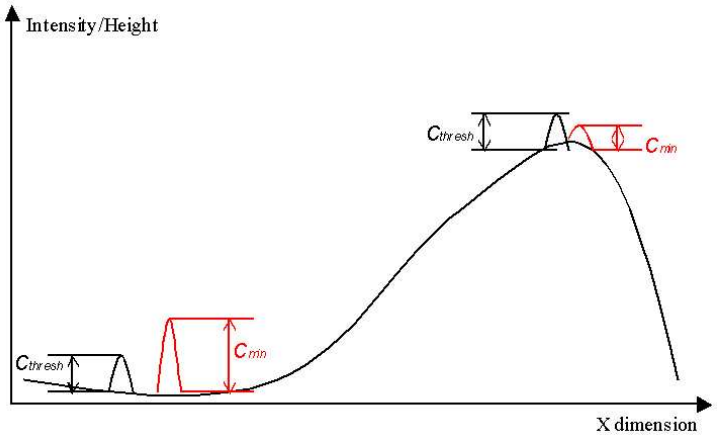

Figure 17: The adaptive qualities of the HVS model. The threshold C_{min}changes according to the values in its immediate neighbourhood and the mean intensity of the image.

$$C_{min} = \frac{c_{mpc}}{\mu_N} \left(b + \sqrt{\frac{\mu_N^2}{\mu_A}} \right)^2 \quad (3)$$

There are a number of parameters involved at this stage. Relevant for our application are the size of the fovea and the minimal perceivable contrast of the human visual system (HVS) model. Empirically, we noted that activations in deep grey matter are not very small, as they usually involve a significant surface of the putamen, head of caudate or thalamus. We set the size of the kernel of fovea to 15x15 pixels to be able detect small enough areas of hyperintensity, but large enough not to depict high frequency noise. As argued in [23], the minimal perceivable contrast must be computed as a function of the image gradient in order to accommodate all possible variations of contrast. In MR images of the brain, the intensity values of GM, WM and CSF can be regularised by intensity normalisation. Therefore, hyperintensities can be regarded as an exception to the normal intensity distribution. In this particular case, the minimal perceivable contrast can be constant over the whole collection of images.

4 Results

4.1 Paris Data

In this first part of the section, we show examples of detection of abnormal hyperintensities in FLAIR MRI on images from patients suffering from CJD collected at the Piti\'e-Salp\'^etri\'ere Hospital in Paris. We employ T1-weighted (TE=20, TR=500), T2-weighted (TE=92, TR=3000) and FLAIR-T2 (TE=148.5, TR=10002, TI=2200) MR images acquired using a GE Signa scanner. Our database comprises 6 patient specific images with histologically proven CJD-related prion infection (3 sporadic CJD, 1 genetic CJD with codon 200 mutation, 1 Gertsmann Straussler-Scheinker (GSS) disease and 1 familial fatal insomnia (FFI)). For each patient we have a T1-weighted, a T2-weighted and a T2 FLAIR sequence. In the examples shown below, we used all three MR imaging sequences for the registration of images and segmentation of hyperintensities. A review of the different stages of our algorithm is shown in Figure 18.

The main areas of interest in CJD are the basal ganglia. Using the mask of internal nuclei , we focused on these structures and did not take into account signal abnormalities in other brain regions, such as white matter high signals that are known to correlate with age and vascular risk factors.

Figure 19 shows detection results on three patients suffering from sporadic CJD. The diagnosis is confirmed by histological examinations. The main radiological characteristic of sporadic forms of CJD diseases is the presence of higher intensities in the caudate nuclei and putamen, while the thalami are less, if at all, affected. Visually, the first two patients presented in Figure 19 comply to this general rule, while the third one has high intensities

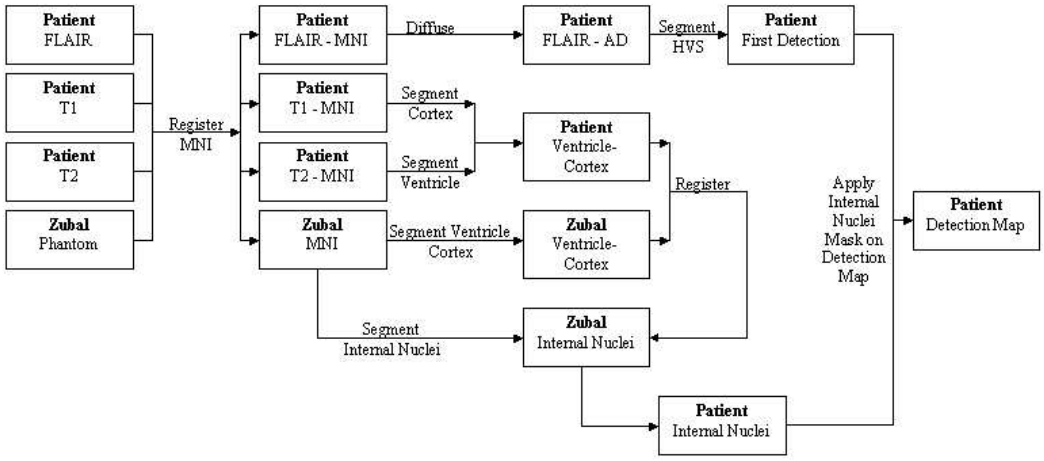

Figure 18: Flowchart of the algorithm proposed for the detection of CJD-related abnormal hyperintensities in multisequence MRI of the brain.

(in red) in the thalami as well. Also, we note the asymmetry of high signals in the second two cases in Figure 19. We consider an intensity being significantly higher than another when their subtraction is superior in absolute value to the difference between the mean intensity over all putamen and caudate nuclei and the mean intensity over all thalami in the database. With the tools developed in this study, we can perform what seems to be the first computer-aided quantitative analysis between intensities in caudate nuclei or putamen, on one hand, and thalami, on the other hand, for CJD patients. We will refer to it as intensity quantification study (IS). In a similar manner to the segmentation and registration of internal nuclei presented in Section 3.2, we create masks of the putamen, caudate nuclei and thalamus from the Zubal Phantom registered on the MNI template (see Figure 23). Using the deformation fields of the Zubal ventricles on the patient ventricles, we align the masks of the three groups of nuclei on the patient images and segment these three anatomical regions on each patient FLAIR image. We prefer using FLAIR images before intensity normalisation. First, the raw image intensities will give the most accurate estimation of mean values in the segmented internal nuclei. To show the accuracy of our intensity normalisation, we also present the FLAIR intensities after normalisation. See Tables 1 and 2 for estimations of mean values and standard deviations before and after intensity normalisation. The results in Tables 1 and 2 are consistent over the sporadic CJD patients and conform to the clinical observations.

A second detection example is shown on data from a patient with genetic CJD. The FLAIR of this dataset is severely hindered by the motion of patient in the MR scanner, as evident by the ghosting artefacts apparent in Figure 20. There are faint signs of hyper-

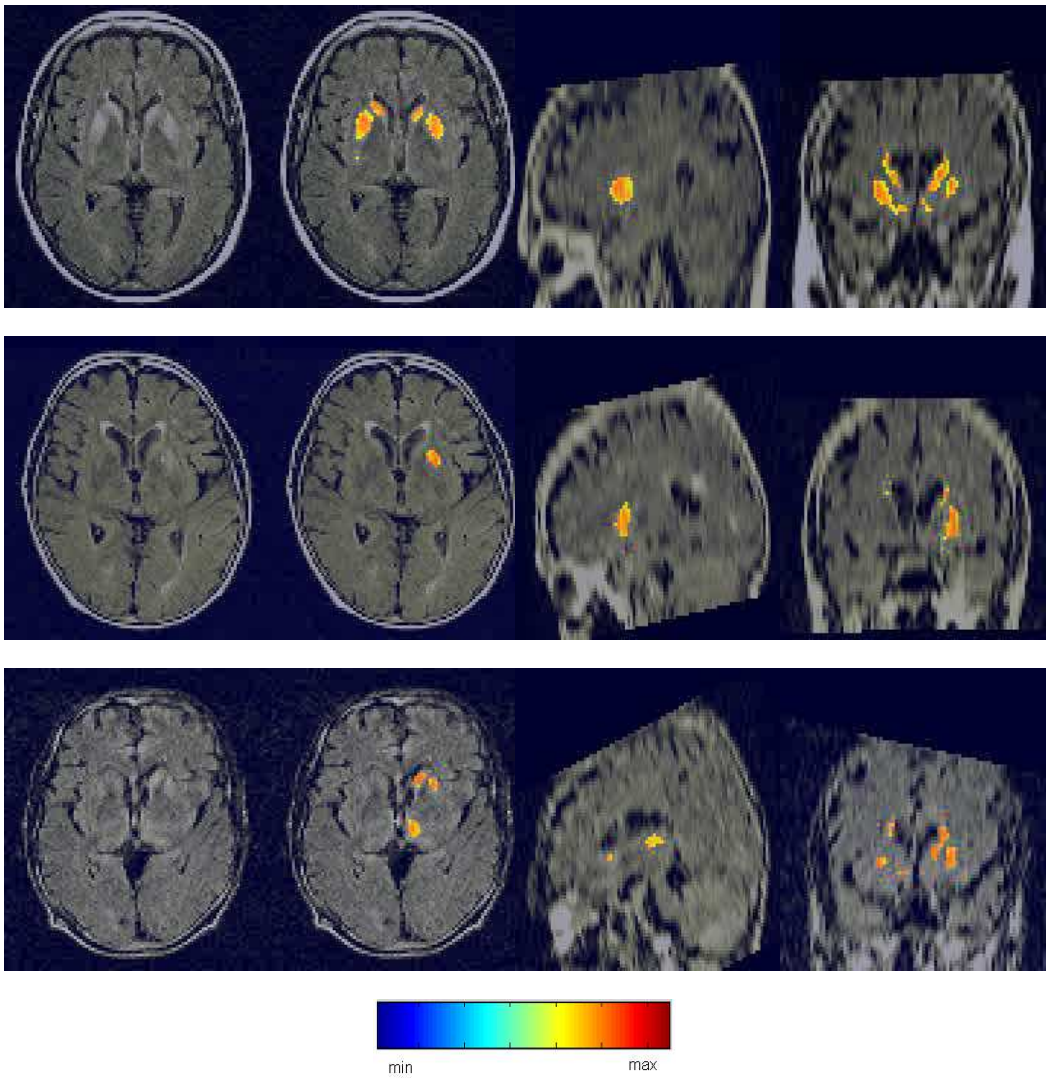

Figure 19: Results on patient data. All three sets of images reported above (one row by case) originate from patients with histologically proven sporadic CJD. We present on the left a cross-section of the FLAIR MR data with abnormal hyperintensities in the internal nuclei; next to it we have the CJD detection map with corresponding intensities, as seen in the attached colourmap; further to the right, we present a sagittal cross-section and a coronal cross-section with their detection maps.

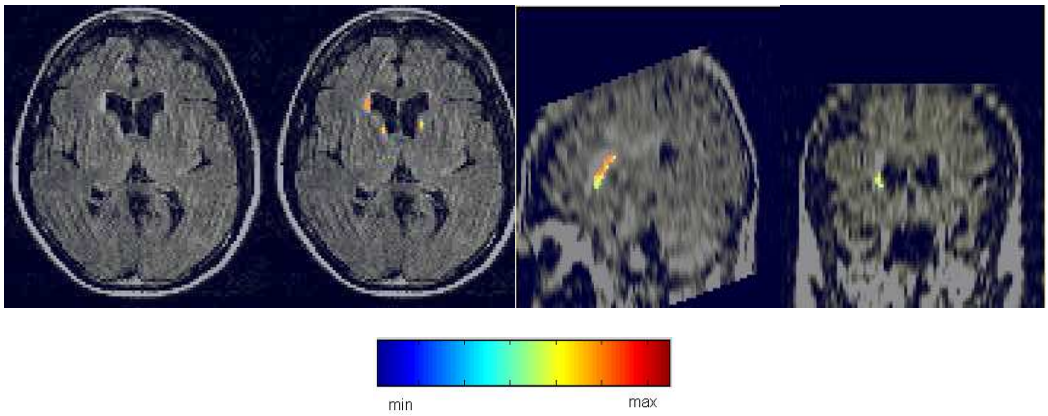

Figure 20: Results on image data from a patient suffering of genetic CJD with codon 200 mutation. The high intensities in the zone of interest are severely hampered by the presence of significant motion artefacts.

intensity in the head of caudate, but these are difficult to interpret due to the movement artefacts. The intensities are also on the lower scale. Table 1 shows no important difference between mean intensities in thalami and putamen or caudate nuclei

In Figure 21, we present two FLAIR MR slices from patients having FFI and GSS. None of them presents abnormal intensities in the internal nuclei, neither does our algorithm detect any. No FP are reported for either of the cases. For the GSS patient, there is no significant difference between intensities in thalami and putamen, while the caudate nuclei show higher signals, but standard deviations are on the lowest scale for the database we analyse. Surprisingly, there is a significantly higher mean intensity in the thalami and caudate nuclei of the FFI patient when compared to that of its putamen. However, the overall mean intensity in thalami is not remarkably different than that of putamen and caudate nuclei together. The standard deviations are small and no signal is highlighted out as abnormal. This is in concordance with the ground truth clinical observation, where clinicians acknowledged the lack of high intensities in the corresponding FLAIR images.

Another case that we bring to the attention of the reader is of a patient with a severe brain atrophy. The patient was initially included in the CJD database, but the histological tests proved that this is not a case of prion infection. The radiological exam found areas of possible stronger intensity in the pulvinar, which combined with the signs of dementia lead to an obvious case for a FP for CJD diagnosis. Our detection algorithm also detected abnormal areas in the pulvinar, but of low intensity. Nevertheless, the case is valuable for testing the non-rigid deformation in this extreme case between the Zubal Phantom ventricles and the large ventricles of this patient, as seen in Figure 13. While there are small abnormalities in the patient's MRI, its data could not be included in the control database.

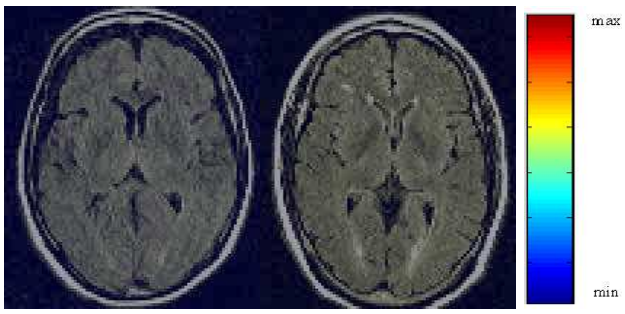

Figure 21: Results on image data from two patients suffering of FFI (left) and GSS (right). Our detection algorithm does not detect any abnormal intensities in the internal nuclei of these patients, as expected.

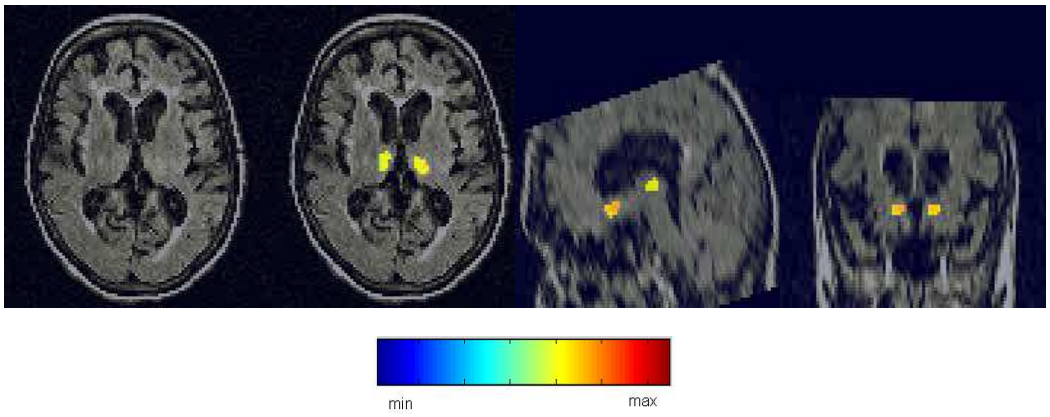

Figure 22: Results on image data from a patient presenting a significant brain atrophy. The patient was suspect of CJD after the radiological examination, but the histological results proved that there is no prion infection present. There are still high intensities (of a lower scale) in the thalami, as our detection algorithm reflects correctly.

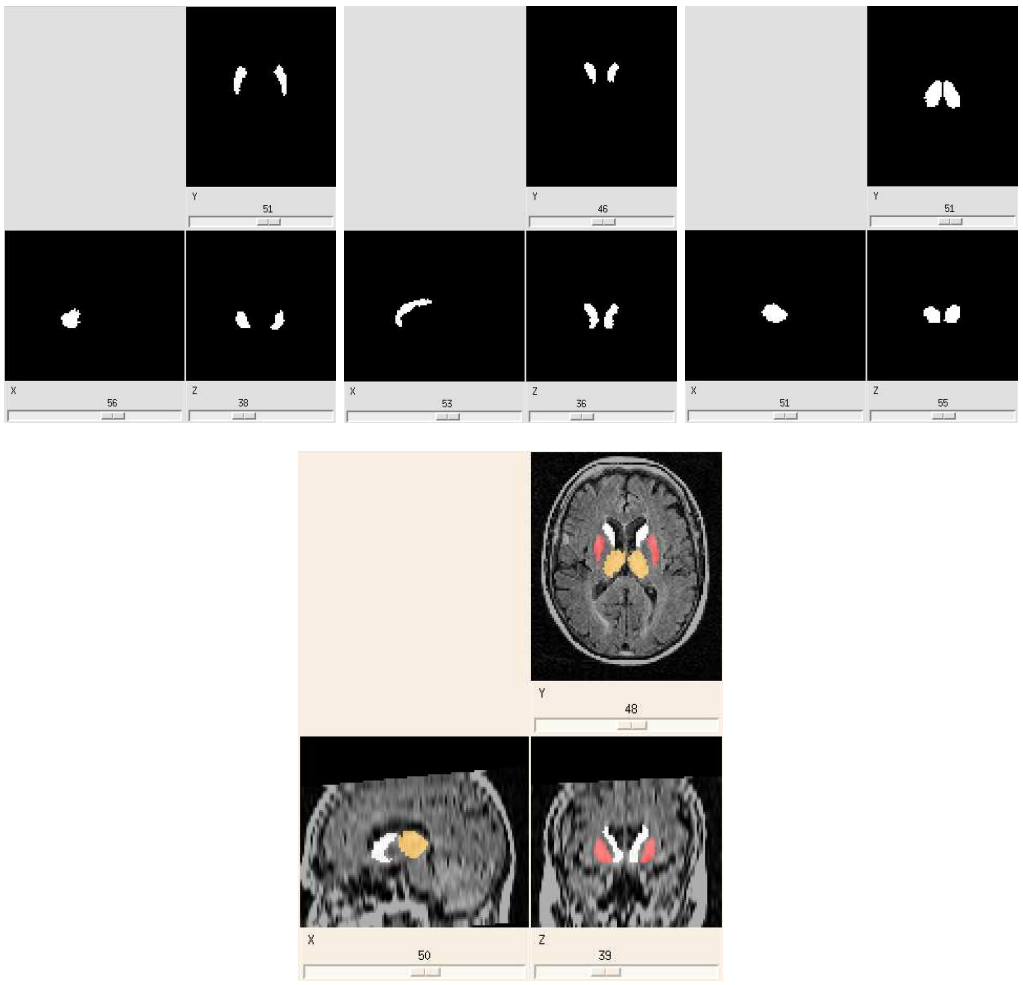

Figure 23: Segmenting the putamen, caudate nuclei and thalami in patient FLAIR images. The first mask on the left is the Zubal putamen mask; the mask in the middle is the Zubal caudate nuclei mask; the mask on the right shows the segmentation of thalami on the Zubal atlas; on the bottom row we have the results of segmentation of putamen, caudate nuclei and thalami on the patient FLAIR image (putamen in red, caudate nuclei in white and thalami in orange) after non rigid registration between the Zubal and patient ventricles.

CJD Type	THALAMUS		PUTAMEN		CAUDATE	
	Original FLAIR		Original FLAIR		Original FLAIR	
	Mean	STD	Mean	STD	Mean	STD
PS001- sp	101.3211	17.5972	**124.9429**	21.1225	**124.2278**	27.4369
PS005 - sp	124.4844	22.8243	**136.4809**	31.0321	**140.0176**	42.3238
PS006 - sp	104.3543	33.0801	110.4657	20.7253	**117.8042**	27.3066
PS002 -gen	130.5156	23.4608	128.1734	21.6547	131.6033	37.0938
PS003 -FFI	**119.3189**	20.9794	106.8575	20.0263	**119.0910**	23.2898
PS007 -GSS	101.7339	16.3646	100.3442	15.2995	**110.9940**	21.1924

Table 1: Mean and standard deviation values in putamen, caudate nuclei and thalami for the Paris Piti\'e-Salp\^etri\'ere patient data. We present results on images before intensity normalisation in order to preserve the original intensity values. The superior mean values are in red (when the difference between putamen or caudate and thalamus mean intensities is greater than 7). All the sporadic data ("sp") shows higher intensities in the putamen or caudate (usually both), which verifies the reports in literature. The genetic case ("gen:, with high motion artefacts) shows no significant differences and has no abnormal intensities in the internal nuclei. The FFI case shows superior values for thalami and caudate nuclei than putamen, although there are no local hyperintensities present in any nuclei and the overall mean intensity in thalami is not importantly different than that of putamen and caudate nuclei together. The GSS case has higher mean intensities in the caudate nuclei, but small standard deviations.

CJD Type	THALAMUS		PUTAMEN		CAUDATE	
	Normalised FLAIR					
	Mean	STD	Mean	STD	Mean	STD
PS001 - sp	141.1449	26.3250	**176.0121**	30.3038	**166.8506**	46.9915
PS005 - sp	124.4844	22.8243	**136.4809**	31.0321	**140.0176**	42.3238
PS006 - sp	144.8648	33.0569	143.7222	27.7494	**154.6807**	40.4034
PS002 - gen	136.6302	25.1715	134.0595	23.3350	137.4741	39.9669
PS003 - FFI	**135.0674**	24.7285	120.5637	23.6229	**134.2546**	27.9160
PS007 - GSS	129.8162	22.5953	128.8745	20.1647	**142.2849**	28.4768

Table 2: Mean and standard deviation values in putamen, caudate nuclei and thalami for the Paris Piti\'e-Salp\^etri\'ere patient data after intensity normalisation. The superior mean values are in red (when the difference between putamen or caudate and thalamus mean intensities is after intensity normalisation greater than 8). The intensity study on normalised data shows identical results to that on the original intensities (see Table 1), which verifies the accuracy of the normalising process that we employ.

4.2 Marseille Data

In the second part of the results section, we show examples of detection of abnormal hyperintensities in FLAIR MRI on images from patients suffering from CJD collected at the Timone Hospital in Marseille. We employ T1-weighted (TE=15, TR=644), T2-weighted (TE=22, TR=4000) and FLAIR-T2 (TE=110, TR=8000, TI=2200) MR images acquired using a Siemens Magnetom Vision scanner. Our database comprises 4 patient specific images, which have histologically proven sporadic CJD, and 3 controls, which are used for the validation of the algorithm. Each patient or control has three images assigned: a T1-weighted, a T2-weighted and a T2 FLAIR sequence that are used for the registration of images and segmentation of hyperintensities.

We employ the same algorithm as in the previous section on Paris data; its stages are shown in Figure 18. In Figure 24, we present the detection maps on patient images with hyperintensities in basal ganglia. All sporadic CJD patients from the Marseille database show abnormal signal deviations in the internal nuclei, although at different extent. The detection results are accurate over the control images, where no hyperintensities are present nor signalled by our algorithm, as further seen in Figure 25. The findings of the intensity quantification study over the data from Marseille are shown in Table 3. As expected, there is no significant difference between mean intensities in putamen/caudate nuclei versus thalami for our control data. However, there is a clear differentiation between the mean intensities in caudate nuclei and thalami in the patient data, while the putamen also show higher intensities than the thalami for two patients only.

The detection of abnormal intensities in basal ganglia are consistent over both databases from Paris and Marseille, although the acquisition protocols vary, as well as the MR scanners used to obtain the data. Through spatial registration and intensity normalisation, our algorithm is not sensitive to imaging conditions in the acquisition and offers good results over various data collections.

4.3 ADC Analysis

The multisequence image acquisition protocol that we employed allowed us to explore the information contained in the apparent diffusion coefficient (ADC) maps of each patient data. The ADC values represent the average diffusion and can be expressed as the mean of the eigenvalues of the diffusion tensor at each voxel of the brain [19, 32]. Their computation was done using the diffusion tensor images (DTI) [39], which were included in the acquisition protocol (TE=91, TR=5300 for Paris data and TE=100, TR=6000 for Marseille data). Thus, the ADC values refer to the mobility of water in an area, which become a tissue specific measure. In an application of our type, theoretically, the ADC should to be able to discriminate gliosis and spongiform changes occurring with the accumulation of prion protein [2, 17].

The ADC maps are computed directly from the raw DTI images. Once the map computed, it is registered to the MNI atlas, as in 2.2.1. We use the deep grey nuclei segmented from the Zubal Phantom and registered to the patient data, see Sections 3.2 and 4.1, to

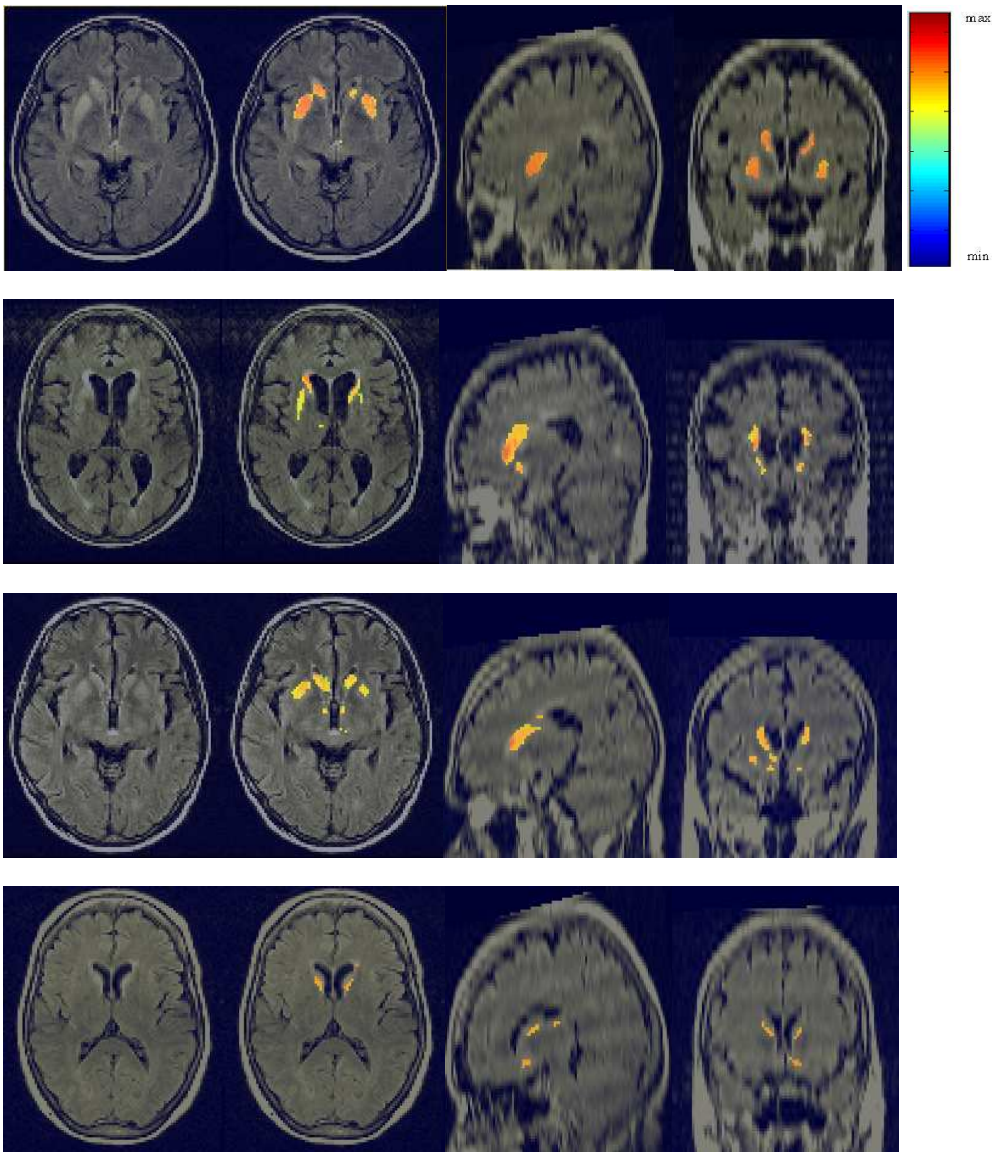

Figure 24: Results on Marseille patient data. All four sets of images reported above (one row by case) originate from patients with histologically proven sporadic CJD. We present on the left a cross-section of the FLAIR MR data with abnormal hyperintensities in the basal ganglia; next to it we have the CJD detection map with corresponding intensities, as seen in the attached colourmap; further to the right, we present a sagittal cross-section and a coronal cross-section with their detection maps. All four image sets present abnormal intensity distributions in the deep grey nuclei, which are correctly detected by our method.

Patient	THALAMUS		PUTAMEN		CAUDATE	
	Original FLAIR					
	Mean	STD	Mean	STD	Mean	STD
MT001 – sp	395.2914	60.9558	**467.6018**	62.8236	**488.1877**	93.2875
MT008 – sp	347.7698	68.2656	**400.1305**	62.6769	**448.5681**	108.5990
MT009 – sp	334.9456	50.1386	356.1703	50.5199	**403.1971**	82.3212
MT012 - sp	361.9343	45.3583	373.2009	45.3734	**411.4626**	70.3560
TM001	363.7554	47.6175	360.5137	42.8949	383.3287	64.7482
TM002	367.6599	46.6720	369.1954	38.5165	394.8521	64.7379
TM004	376.3989	52.3517	365.2786	39.9349	391.1589	59.3861

Table 3: Mean and standard deviation values in putamen, caudate nuclei and thalami for the Marseille La Timone patient data. We present results on the original images, where MT refers to a CJD patient, while TM to a control. The superior mean values are in red (when the difference between putamen or caudate nuclei and thalami mean intensities is greater than 28, the equivalent of the previous value of 7 for Paris data adapted to the new database). All sporadic CJD patients have significantly higher mean intensities in the caudate nuclei and less frequent in the putamen versus thalami. Mean MR intensities in control data grey nuclei are homogeneous.

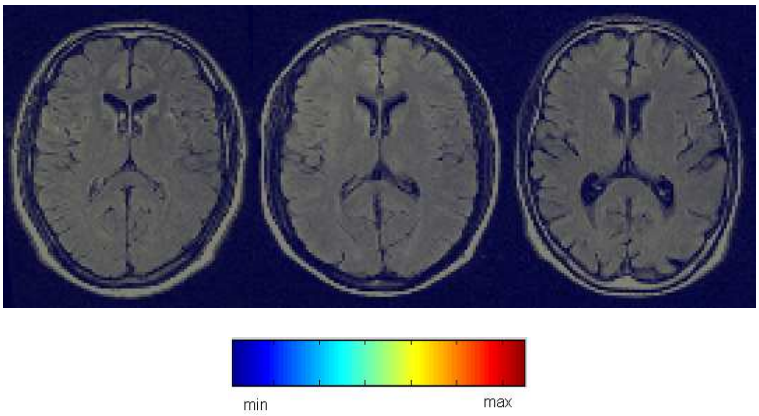

Figure 25: Results on control images from the Marseille database. We show three images of controls, where our algorithm does not signal any false positives (FP).

localise the putamen, thalami and caudate nuclei in the ADC maps (Figure 26). The ADC mean values and standard deviations of both Paris and Marseille data are presented in Tables 4 and 5. A clearer comparison between groups of patients and controls is shown in Table 6.

In the Paris database we have no controls to date, therefore we compare mean ADC values between groups of patients. While the genetic and GSS patients have more homogeneous ADC values over the deep grey nuclei, the genetic patient has higher mean ADC values than the other patients in the database. The most outstanding ADC values appear in the putamen of sporadic CJD patients (which are low and could be related to spongiform changes) and the thalami of the FFI patient (which is very high and probably corresponds to gliosis). Comparing controls with sporadic cases over the Marseille database, the effects of spongiform changes become evident, as mean ADC values both in putamen and caudate nuclei are lower in sporadic patients. As in the intensity study in FLAIR images, the ADC values analysis confirm in a quantitative form the previous neuroradiological observation regarding the tissue changes in the brain of prion disease patients.

5 Discussions

The results presented in Tables 1, 2 and 3 represent a first attempt for quantitative numerical analysis of in FLAIR-T2 images MR intensities of thalamus versus putamen and caudate nucleus in CJD patients. They accurately quantify the clinical remarks related to the possible classification of different types of human spongiform encephalopathies.

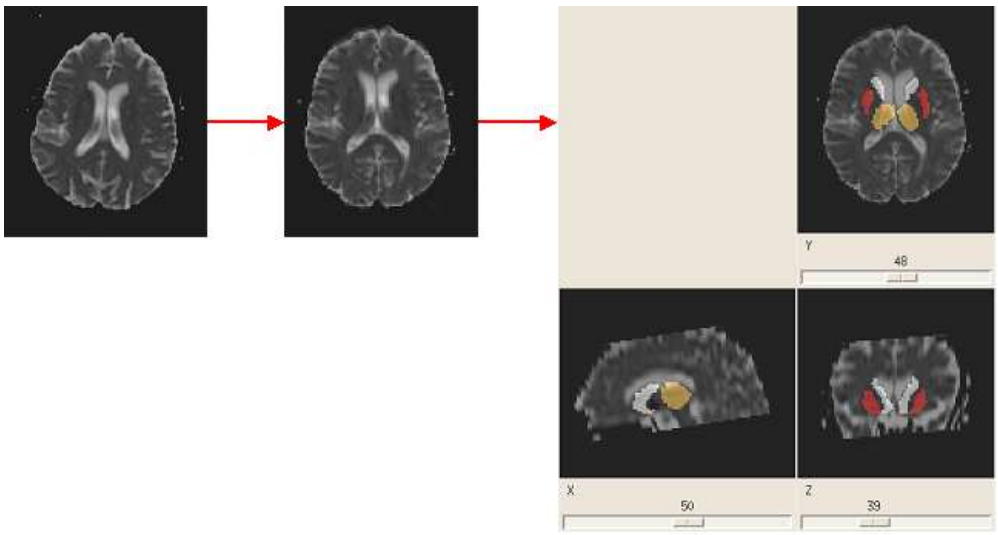

Figure 26: Segmenting the putamen, caudate nuclei and thalami in patient ADC images. From left to right: the original patient ADC image computed from the DTI images; the patient ADC images registered to the MNI atlas; the results of segmenting the putamen, caudate nuclei and thalami on the patient ADC image (putamen in red, caudate nuclei in white and thalami in orange) after the deformation of the Zubal deep grey nuclei on patient data.

CJD Type	THALAMUS		PUTAMEN		CAUDATE	
	Original ADC x 10^{-6}					
	Mean	STD	Mean	STD	Mean	STD
PS001-sp	789.3085	189.2742	691.9228	171.8785	841.7771	243.6028
PS005-sp	844.914	175.3900	797.2171	150.4142	903.9285	259.1414
PS006-sp	780.1928	224.6700	721.3242	161.8071	779.1042	301.7885
PS002-gen	904.5471	175.6214	906.3057	151.4771	940.9500	229.6600
PS003-FFI	1114.1786	229.9200	923.7914	266.7400	935.4171	261.6300
PS007-GSS	830.8700	167.3514	810.5242	147.4328	829.7014	190.5442

Table 4: ADC mean and standard deviation values in putamen, caudate nuclei and thalami for the Paris La Piti\'e-Salp\^etri\'ere patient data (in mm^2/s). "Sp" refers to a sporadic CJD patient, while "gen" to a genetic CJD patient. The ADC mean values in the putamen of sporadic CJD patients are constantly lower than in the corresponding thalami or caudate nuclei. For the FFI case, the thalami mean ADC value is significantly superior to those of patient's caudate nuclei and putamen. These differences are better underlined in Table 6.

Patient	THALAMUS		PUTAMEN		CAUDATE	
	Original ADC x 10^{-6}					
	Mean	STD	Mean	STD	Mean	STD
MT001 – sp	766.085	124.976	646.871	166.586	720.383	180.167
MT008 – sp	740.209	132.946	758.650	122.097	764.503	161.362
MT009 – sp	762.603	106.461	732.405	86.045	744.704	147.935
MT012 – sp	793.267	102.734	787.959	90.478	765.651	135.760
TM001	747.573	103.911	757.660	76.731	773.316	126.36
TM002	793.378	95.533	814.132	68.691	794.187	126.902
TM004	792.391	95.020	816.186	76.019	828.238	102.971

Table 5: ADC mean and standard deviation values in putamen, caudate nuclei and thalami for the Marseille La Timone patient data (in mm^2/s). MT refers to a CJD patient, while TM to a control. For the Marseille data, there is no obvious repetitive discrimination between the ADC values in one patient's putamen, caudate nuclei and thalami. Differences become clearer when we compare mean ADC values in sporadic CJD patients versus controls, as in Table 6.

CJD Type PS Data	THALAMUS		PUTAMEN		CAUDATE	
	Original ADC x 10^{-6}					
	Mean	STD	Mean	STD	Mean	STD
Sporadic x3	804.805	196.444	**736.823**	161.366	841.601	268.177
Genetic	904.547	175.621	906.305	151.477	940.950	229.660
FFI	**1114.178**	229.920	923.791	266.740	935.417	261.630
GSS	830.870	167.351	810.524	147.432	829.701	190.544

CJD Type MT Data	THALAMUS		PUTAMEN		CAUDATE	
	Original ADC x 10^{-6}					
	Mean	STD	Mean	STD	Mean	STD
Sporadic x4	764.260	116.779	**742.463**	116.301	**754.485**	156.306
Normal	777.712	98.154	795.933	73.813	798.560	118.744

Table 6: Comparative ADC mean values for groups of patients and controls. On the top, we present results on the Paris patients. We note the lower ADC mean values in the putamen of sporadic CJD patients (which could be the effect of spongiform changes), while the thalami of the GSS patient show much higher values than the rest of the database (presumably associated with the presence of gliosis). On the bottom, we show results on the Marseille database, where we compare mean ADC values between patients and controls. As expected, the mean ADC values in patients putamen and caudate nuclei are inferior to those of normals, where ADC values are more homogeneous over the deep grey nuclei.

All Paris sporadic CJD patients have higher mean intensities in the caudate nuclei and generally putamen, as expected, although there are hyperintensities present in the thalami too. There is no significant difference between the mean intensities in the Paris genetic case, whereas there are hyperintensities present in its MRI. Small differences are also present in the Paris GSS case, but only in the caudate nuclei. The only case with superior mean intensity in the thalami over putamen is the Paris FFI patient, but no hyperintensities are present in this MRI, as the mean over thalami is not significantly higher over the mean of putamen and caudate nuclei together. All our experimental results are in complete accordance with the neurological findings in clinical practice and with the brain lesions profile described in each form of the disease.

The same rule applies to the Marseille sporadic CJD patients: higher mean intensities in the caudate nuclei and less frequently in the putamen versus the thalami. All four sporadic patients show abnormal intensities in the deep grey nuclei, which are correctly detected by our algorithm. As we do not detect any hyperintensities in controls basal ganglia, we neither find significant differences between the mean intensities in the three deep grey nuclei of interest (thalamus, caudate nucleus and putamen).

Similarly, we quantify the mean ADC values in the deep grey nuclei. Once more we confirm the visually-based clinical observations, according to which we should expect lower ADC values in caudate nuclei and putamen of sporadic CJD cases, which could be due to spongiform changes. An interesting finding was the increased mean ADC value in the thalami of the FFI patient, which could probably correspond to the intense thalamic gliosis usually observed. More on the ADC quantification will be done when control data will be available from Paris.

In order to decrease the number of FP prompted by our detection algorithm, we refined the registration of the segmented data (the Zubal Atlas) on the patient specific data. Although we prefer the results using masks of the ventricles and cortex outer boundary (see Section 3.2), we also tested the use of masks of only ventricles (therefore without regularising the deformation within the brain). An example is shown in Figure 27 with a clear outperformance in the case using the brain boundary, where FP are removed and the pulvinar intensities are more accurately detected. We further show in Figure 28 an example of detection without employing the smoothing procedure presented in Section 2.3. Once more, the results are superior when noise is removed preserving edges and FP are eliminated.

We collected two series of results: one from the foveal segmentation of hyperintensities in the basal ganglia; and a second from the intensity quantification study of intensity differences between putamen/caudate nuclei versus thalami. Although we have 10 patients with histologically proven prion diseases, only 8 of them show hyperintensities in the basal ganglia, according to the ground truth. Thus, our database comprises 10 patients and 3 controls, from which 8 MRI sets show hyperintensities in the zone of interest. The validation results are presented in Table 7. With a combination of foveal segmentation and intensity quantification, we are able to prompt 10/10 prion disease cases, with or without hyperintensities present in the basal ganglia. No FP are found amongst the controls. We

detect all cases of hyperintensities in the basal ganglia employing the foveal segmentation of signal deviations.

We investigated the response of well known algorithms, such as voxel-based morphometry (VBM) [1] and expectation-maximization segmentation (EMS) [36], on detecting CJD-related abnormalities in brain MRI. The good contrast between brain structures is essential in statistical-based methods. Hence, the performance of EMS and VBM on CJD patient data, which have important artefacts and no contrast between grey matter and white matter, is inconsistent and irrelevant for clinical applications. Registration errors also influence the quality of statistical results, as comparisons between equivalent areas in normals versus patients or between different groups of patients are very sensitive to the correct delineation of the regions of interest.

A good balance between the sensitivity and specificity of results is highly desirable in any computer-aided diagnosis (CAD) algorithm. In Figure 29, we show comparative results obtained by varying the minimal perceivable contrast (see Section 3.3) for better specificity or sensitivity. In future work, we will perform a receiver operating characteristic (ROC) curve analysis of detection results. The effect of partial volume effects (PVE) [15] will also be investigated for removal of FP, along with the improved segmentation of ventricles by phase congruency (PC) [22]. We will also explore further quantitative analysis of MRI intensities for discriminating between the different types of human spongiform encephalopathy, when more patient data are available.

The detection of deep grey nuclei hyperintensities confirms the previous visually-based clinical observations according to which the FLAIR/T2 MR images of sporadic CJD patients show hypersignals in the caudate nuclei. Quantifying the intensities in thalami, caudate nuclei and putamen, we prove that there are always higher mean intensities in the caudate nuclei (7/7) and sometimes putamen (4/7) than the thalami for the same sporadic CJD patients. This conclusion highlights the caudate nuclei as area of interest for the diagnosis of CJD, in complete agreement with the neuropathological findings. The relevance of caudate nuclei is also underlined by the decreased quantified mean ADC values in patient versus normal data. With zero FP, our method of detection and quantification of basal ganglia intensity distributions proves to reach maximum specificity with very high sensitivity.

6 Conclusion

We presented a method for the detection of hypersignals in grey matter internal nuclei from multisequence MR images. The particular context of our application aims to indicate the presence of human spongiform encephalopathies, prion protein diseases here referred as Creutzfeldt-Jakob Diseases (CJD). The technique employs intensity and spatial normalisation, noise removal with feature enhancement, foveal segmentation for the detection of hyperintensities and a priori anatomical information for refined registration and removal of false positives. An intensity quantification study is further developed for better detection results with a view to discriminate between the different types of prion diseases. The detection results are in accordance with the clinical ground truth. Our study demonstrates the value

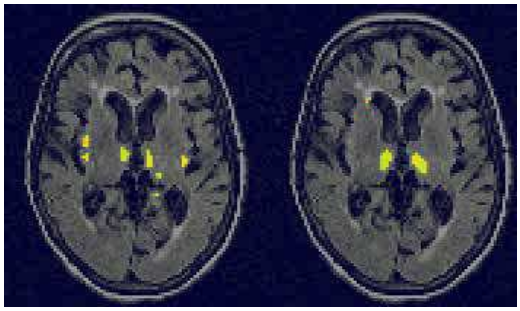

Figure 27: The improved registration at deep grey matter level removes FP while detecting correctly the abnormal signals. On the left, we see the results of detection when only a mask of ventricles was used for the non-rigid registration. On the right, the cortex outer margin is added as an anatomical boundary constraint in computing the deformation fields of the non-rigid registration (see Figure 13).

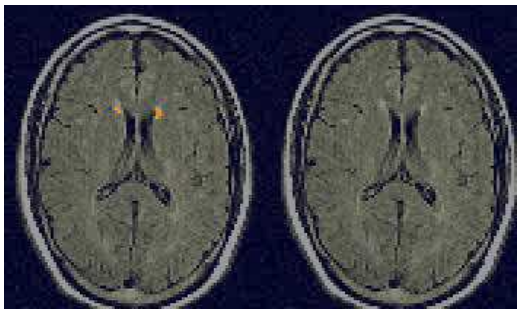

Figure 28: Removal of FP by image smoothing and edge enhancement. On the left, we see the results of detection on an image with no abnormal signal in internal nuclei; we only detect high frequency structures. On the right, the FP are removed after employing anisotropic diffusion as image smoother.

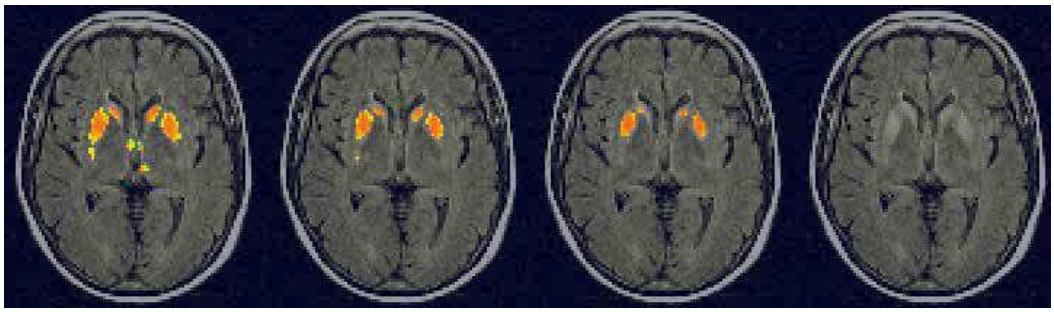

Figure 29: The influence of parameter choice in the segmentation of hyperintensity. Above, we show the same MR slice (in original on further right) with detection maps superimposed. We varied the value of the minimal perceivable contrast for higher sensitivity (further left detection map) and higher specificity (further right detection map). The results presented in Section 4 use the middle choice of minimal perceivable contrast with a good balance between specificity and sensitivity.

	Prion Diseases	Sporadic CJD	Controls	Hyperintensity
Human Visual System (HVS)	8/10	**7/7**	**0/3**	**8/8**
Intensity Study (IS)	9/10	**7/7**	**0/3**	7/8
HVS and IS	7/10	**7/7**	**0/3**	7/8
HVS or IS	**10/10**	**7/7**	**0/3**	**8/8**

Table 7: The validation of our algorithm. We present detection results using: (i) the foveal segmentation of hyperintensities in basal ganglia (HVS); (ii) the intensity quantification study (IS); (iii) a logical 'and' between HVS and IS; (iv) a logical 'or' between HVS and IS. The best results for each column are highlighted in red. While a combination of HVS and IS gives the best detection results, hyperintensities are also correctly detected by HVS only, and therefore all sporadic CJD cases, the IS is the most sensitive to prion diseases in general, while the number of false positives (FP) is zero.

of MRI for a prospective non-invasive diagnosis of sporadic CJD and the characterisation of prion diseases. More validation will be performed in future work, when a larger database is available.

Our method further allows the quantification of intensity distributions in basal ganglia, a discrimination criterion between patients and normals, which confirms the visually-based radiological observations related to CJD. The caudate nuclei are highlighted as main areas of diagnosis of sporadic CJD, in agreement with the histological data. The caudate nuclei and putamen show more significant hypersignal than in thalami in sporadic CJD patient FLAIR data. The relevance of caudate nuclei and putamen is also underlined by their decreased quantified ADC values in patient versus normal data, probably due to the accumulation of pathological prion protein.

In this preliminary study, our method proves as reliable as the interpretation of radiologists for the detection of basal ganglia hypersignals. Moreover, it allows to automatically obtain quantitative data from MR patients with CJD, which could be used for the follow-up, whether a treatment is available or not.

Acknowledgements

This work is funded by the GIS-Prions project (see the partaking centres under the authors names) coordinated by Jean-Philippe Brandel.

References

[1] J. Ashburner and K.J. Friston. Voxel-based morphometry - the methods. *NeuroImage*, 11:805–821, 2000.

[2] M.M. Bahn, D.K. Kido, W. Lin, and A.L. Pearlman. Brain magnetic resonance diffusion abnormalities in imaging in creutzfeldt-jakob disease. *Arch Neurol*, 54:1411–1415, 1997.

[3] M.M. Bahn and P. Parchi. Abnormal diffusion-weighted magnetic resonance images in Creutzfeldt-Jakob disease. *Arch Neurol*, 56:577–583, 1999.

[4] J.P. Brandel. Clinical aspects of human spongiform encephalopathies, with the exception of iatrogenic forms. *Biomed Pharmacother*, 53:14–18, 1999.

[5] J.P. Brandel, N. Delasnerie-Laupretre, J.L. Laplanche, J.J. Hauw, and A. Alpetrovitch. Diagnosis of Creutzfeldt-Jakob disease: Effect of clinical criteria on incidence estimates. *Neurology*, 54:1095–1099, 2000.

[6] M A. Brown and R.C. Semelka. MR imaging abbreviations, definitions, and descriptions: A review. *Radiology*, 213:647–662, 1999.

[7] P. Cachier, E. Bardinet, D. Dormont, X. Pennec, and N. Ayache. Iconic feature-based nonrigid registration: The PASHA algorithm. *CVIU — Special Issue on Nonrigid Registration*, 89(2-3):272–298, Feb.-March 2003.

[8] D.L. Collins, A.P. Zijdenbos, V. Kollokian, J.G. Sled, N.J. Kabani, C.J. Holmes, and A.C. Evans. Design and construction of a realistic digital brain phantom. *IEEE Transactions on Medical Imaging*, 17(3):463–468, 1998.

[9] A. Coulthard, K. Hall, P.T. English, P.G. Ince, D.J. Burn, and D. Bates. Quantitative analysis of mri signal intensity in new variant Creutzfeldt-Jakob disease. *The British Journal of Radiology*, 72:742–748, 1999.

[10] J.A. de Priester, G.H. Jansen, J.R. de Kruijk, and J.T. Wilmink. New MRI findings in Creutzfeldt-Jakob disease: High signal in the globus pallidus on T1-weighted images. *Neuroradiology*, 41:265–268, 1999.

[11] P. Demaerel, A. Baert, W. Vanopdensboch, and R. Robberecht. Diffusion weighted magnetic resonance imaging in Creutzfeldt-Jakob disease: Research letter. *The Lancet*, 349:847–848, 1997.

[12] D. Dormont. New variant of Creutzfeldt-Jakob disease. *Euro Surveil*, 5(9):95–97, 2000.

[13] M. Finkenstaedt, A Szudra, I. Zerr, S. Poser, J. Hise, J. Stoebner, and T. Wener. MR imaging of Creutzfeldt-Jakob disease. *Radiology*, 3:793–798, 1991.

[14] H.J Gertz, H. Henkes, and J. Cervos-Navarro. Creutzfeldt-jakob disease: Correlation of MRI and neuropathologic findings. *Neurology*, 38(9):1481–1482, 1988.

[15] M. A. González Ballester, A. Zisserman, and M. Brady. Estimation of the partial volume effect in MRI. *Medical Image Analysis*, 6(4):389–405, 2002.

[16] S. Haik, J.P. Brandel, C. Oppenheim, V. Sazdovitch, J.J. Dormont, D. Hauw, and C. Marsault. Sporadic CJD mimicking variant CJD with bilateral increased signal in the pulvinar. *Neurology*, 58:148–149, 2002.

[17] S. Haik, D. Dormont, B.A. Faucheux, C. Marsault, and J.J. Hauw. Prion protein deposits in magnetic resonance imaging signal abnormalities in Creutzfeldt-Jakob disease. *Annals of Neurology*, 51(6):797–799, June 2002.

[18] J P. Hornak. The basics of MRI. http://www.cis.rit.edu/htbooks/mri/.

[19] E.W. Hsu and S. Mori. Analytical expressions for the nmr apparent diffusion coefficients in an anisotropic system and a simplified method for determining fiber orientation. *Magnetical Resonance in Medicine*, 34:194–200, 1995.

[20] D.E. Job, S. Whalley, H.C. ad McConnell, M. Glabus, E.C. Johnstone, and S.M. Lawrie. Structural gray matter differences between first-episode schizophrenics and normal controls using voxel-based morphometry. *Neuroimage*, 17:880–889, 2002.

[21] G.B. Karas, E.J. Burton, S.A.R.B. Rombouts, R.A. van Schijndel, J.T. O'Brien, P. Scheltens, I.G. McKeith, D. Williams, C. Ballard, and F. Brakhof. A comprehensive study of gray matter loss in patients with Alzheimer's disease using optimized voxel-based morphometry. *Neuroimage*, 18:895–907, 2003.

[22] M. G. Linguraru, M. A. González Ballester, and N. Ayache. A multiscale feature detector for morphological analysis of the brain. In Randy E.E. and Terry M.P., editors, *Proc. of MICCAI'03*, volume 2879 of *LNCS*, pages 738–745, Montreal, Canada, nov 2003. Springer Verlag.

[23] M.G. Linguraru. *Feature Detection in Mammmographic Image Analysis.* PhD thesis, University of Oxford, 2002.

[24] J.C. Mazziotta, A.W. Toga, A.C. Evans, P.T. Fox, J. Lancaster, K. Zilles, R.P. Woods, T. Paus, G. Simpson, B. Pike, C.J. Holmes, D.L. Collins, P.M. Thompson, D. MacDonald, M. Iacoboni, T. Schormann, K. Amunts, N. Palomero-Gallagher, S. Geyer, L. Parsors, K.L. Narr, N. Kabani, G. Le Goualher, M. Boomsma, T. Cannon, R. Kawashima, and B. Mazoyer. A probabilistic atlas and reference system for the human brain: International consortium for brain mapping (ICBM). *Philosophical Transactions of the Royal Society of London, Series B (Biological Sciences)*, 356(1412):1293–1322, 2001. Enclosed in Appendix II.

[25] W. Milton, S. Atlas, E. Lavi, and J. Moliman. Magnetic resonance imaging of Creutzfeldt-Jakob disease. *Annals of Neurology*, 29:438–440, 1991.

[26] M. Onofrj, T. Fulgente, D. Gambi, and G. Macchi. Early MRI findings in Creutzfeldt-Jakob disease. *Journal of Neurology*, 240:423–426, 1993.

[27] S. Ourselin. *Recalage d'Images Médicales par Appariement de régions - Application à la Construction d'Atlas Histologiques 3D.* PhD thesis, Université de Nice - Sophia Antipolis, 2002.

[28] S. Ourselin, A. Roche, S. Prima, and N. Ayache. Block matching: A general framework to improve robustness of rigid registration of medical images. In A.M. DiGioia and S. Delp, editors, *Third International Conference on Medical Robotics, Imaging And Computer Assisted Surgery (MICCAI 2000)*, volume 1935 of *Lectures Notes in Computer Science*, pages 557–566, Pittsburgh, Pennsylvanie USA, octobre 11-14 2000. Springer.

[29] G.S. Pearl and R.E. Anderson. Creutzfeldt-jakob disease: High caudate signal on magnetic resonance imaging. *South Med J*, 82:1177–1180, 1989.

[30] D. Rey, G. Subsol, H. Delingette, and N. Ayache. Automatic detection and segmentation of evolving processes in 3D medical images: Application to multiple sclerosis. *Medical Image Analysis*, 6:163–179, 2002.

[31] A. Schroeter, I. Zerr, K. Henkel, and H.J. Tschampa. Magnetic resonance imaging in the clinical diagnosis ofCreutzfeldt-Jakob disease. *Arch Neurol*, 57:1751–1757, 2000.

[32] S. Skare. *Optimisation Strategies in Diffusion Tensor MR Imaging*. PhD thesis, Karolinska University Press, 2002.

[33] D.D. Stark, W.G. Bradley, and W.G. Jr. Bradley. *Magnetic Resonance Imaging*. Mosby, 3rd edition, 1999.

[34] J. Talairach and P. Tournoux. *Co-Planar Stereotaxic Atlas of the Human Brain*. Thieme Medical Publishers, 1988.

[35] H. Urbach, J. Klisch, HK. Wolf, and et al. MRI in sporadic Creutzfeldt-Jakob disease: correlation with clinical and neuropathological data. *Neuroradiology*, 40:65–70, 1998.

[36] K. Van Leemput. *Quantitative Analysis of Signal Abnormalities in MR Imaging for Multiple Sclerosis and Creutzfeldt-Jakob Disease*. PhD thesis, Katholieke Universiteit Leuven, 2001.

[37] K. Van Leemput, F. Maes, D. Vandermeulen, A. Colchester, and P. Suetens. Automated segmentation of multiple sclerosis lesions by model outlier detection. *IEEE Transactions on Medical Imaging*, 20(8):677–688, 2001.

[38] J. Weickert. *Anisotropic Diffusion in Image Processing*. B.G. Teubner, 1st edition, 1998.

[39] C.F. Westin, S.E. Maier, B. Khidhir, P. Everett, F.A. Jolesz, and R. Kikinis. Image processing for Diffusion Tensor Magnetic Resonance Imaging. In *Medical Imaging And Computer Assisted Surgery (MICCAI 1999)*, Lectures Notes in Computer Science, pages 441–452. Springer, 1999.

[40] R.G. Will, M. Zeidler, G.E. Stewart, M.A. Macleod, J.W. Ironside, S.N. Cousens, J. Mackenzie, K. Estibeiro, A.J.E. Green, and R.S.G. Knight. Diagnosis of new variant Creutzfeldt-Jakob disease. *Ann Neurol*, 47:575–582, 2000.

[41] M. Zeidler, R.J. Sellar, D.A. Collie, R.S.G. Knight, G.E. Stewart, M.A. Macleod, J.W. Ironside, S.N. Cousens, A.F.C. Colcester, D.M. Hadley, and R.G. Will. The pulvinar sign on magnetic resonance imaging in variant Creutzfeldt-Jakob disease. *The Lancet*, 355:1412–1418, April 2000.

[42] I.G. Zubal, C.R. Harrell, E.O. Smith, Z. Rattner, G. Gindi, and P.B. Hoffer. Computerized three-dimensional segmented human anatomy. *Medical Physics*, 21:299–302, 1994.

Unité de recherche INRIA Sophia Antipolis
2004, route des Lucioles - BP 93 - 06902 Sophia Antipolis Cedex (France)

Unité de recherche INRIA Futurs : Parc Club Orsay Université - ZAC des Vignes
4, rue Jacques Monod - 91893 ORSAY Cedex (France)
Unité de recherche INRIA Lorraine : LORIA, Technopôle de Nancy-Brabois - Campus scientifique
615, rue du Jardin Botanique - BP 101 - 54602 Villers-lès-Nancy Cedex (France)
Unité de recherche INRIA Rennes : IRISA, Campus universitaire de Beaulieu - 35042 Rennes Cedex (France)
Unité de recherche INRIA Rhône-Alpes : 655, avenue de l'Europe - 38334 Montbonnot Saint-Ismier (France)
Unité de recherche INRIA Rocquencourt : Domaine de Voluceau - Rocquencourt - BP 105 - 78153 Le Chesnay Cedex (France)

Éditeur
INRIA - Domaine de Voluceau - Rocquencourt, BP 105 - 78153 Le Chesnay Cedex (France)
http://www.inria.fr
ISSN 0249-6399